J. Fluid Mech., page 1 of 29.
doi:10.1017/jfm.2012.245

Direct numerical simulation and biglobal stability investigations of the gaseous motion in solid rocket motors

F. Chedevergne[1]‡, G. Casalis[1] and J. Majdalani[2]†

[1] Aerodynamics and Energetics Modelling Department, ONERA, Toulouse 31055, France

[2] Department of Mechanical, Aerospace and Biomedical Engineering, University of Tennessee Space Institute, Tullahoma, TN 37388, USA

(Received 2 October 2011; revised 12 March 2012; accepted 23 May 2012)

In this article, a biglobal stability approach is used in conjunction with direct numerical simulation (DNS) to identify the instability mode coupling that may be responsible for triggering large thrust oscillations in segmented solid rocket motors (SRMs). These motors are idealized as long porous cylinders in which a Taylor–Culick type of motion may be engendered. In addition to the analytically available steady-state solution, a computed mean flow is obtained that is capable of securing all of the boundary conditions in this problem, most notably, the no-slip requirement at the chamber headwall. Two sets of unsteady simulations are performed, static and dynamic, in which the injection velocity at the chamber sidewall is either held fixed or permitted to vary with time. In these runs, both DNS and biglobal stability solutions converge in predicting the same modal dependence on the size of the domain. We find that increasing the chamber length gives rise to less stable eigenmodes. We also realize that introducing an eigenmode whose frequency is sufficiently spaced from the acoustic modes leads to a conventional linear evolution of disturbances that can be accurately predicted by the biglobal stability framework. While undergoing spatial amplification in the streamwise direction, these disturbances will tend to decay as time elapses so long as their temporal growth rate remains negative. By seeding the computations with the real part of a specific eigenfunction, the DNS outcome reproduces not only the imaginary part of the disturbance, but also the circular frequency and temporal growth rate associated with its eigenmode. For radial fluctuations in which the vorticoacoustic wave contribution is negligible in relation to the hydrodynamic stability part, excellent agreement between DNS and biglobal stability predictions is ubiquitously achieved. For axial fluctuations, however, the DNS velocity will match the corresponding stability eigenfunction only when properly augmented by the vorticoacoustic solution for axially travelling waves associated with the Taylor–Culick profile. This analytical approximation of the vorticoacoustic mode is found to be quite accurate, especially when modified using a viscous dissipation function that captures the decaying envelope of the inviscid acoustic wave amplitude. In contrast, pursuant to both static and dynamic test cases, we find that when the frequency of the introduced eigenmode falls close to (or crosses over) an acoustic mode, a nonlinear mechanism is triggered that leads to the emergence of a

† Email address for correspondence: joe.majdalani@gmail.com

‡ Present address: Fundamental and Applied Energetics Department, ONERA, Châtillon, France.

secondary eigenmode. Unlike the original eigenmode, the latter materializes naturally in the computed flow without being artificially seeded. This natural occurrence may be ascribed to a nonlinear modal interplay in the form of internal, eigenmode-to-eigenmode coupling instead of an external, eigenmode pairing with acoustic modes. As a result of these interactions, large amplitude oscillations are induced.

Key words: absolute/convective instability, aeroacoustics, vortex shedding

1. Introduction

Large segmented solid rocket motors (SRMs) are known to exhibit thrust oscillations that can be induced by inevitable disturbances that develop in motor cavities. Efforts to understand and predict the onset of these oscillations continue to receive attention in the propulsion community, particularly in the framework of the P230 programme, the primary booster for the European Ariane 5 launcher (see Fabignon *et al.* 2003). Although resonant combustion and, primarily, acoustic instabilities such as those studied by Culick (1968) and Kuentzmann (1991) were originally believed to be the only causes of thrust oscillations, hydrodynamic instabilities of the flow inside the motor have also been shown to provide additional sources of perturbations.

The earliest contributions in this direction include those by Varapaev & Yagodkin (1969), Beddini (1986), Vuillot (1995), Lee & Beddini (1999, 2000), and others. However, these endeavours have rested on the one-dimensional normal mode approach with perturbations in the streamfunction. Subsequent studies by Casalis, Avalon & Pineau (1998) and Griffond & Casalis (2001) have extended the one-dimensional investigations with the addition of experimental measurements and theoretical solutions based on perturbing the primitive variables. The latter are formulated along the lines of the local non-parallel (LNP) approach, in which all of the non-zero components of the basic flow are retained in the Navier–Stokes equations. In this vein, Casalis *et al.* (1998), Griffond, Casalis & Pineau (2000) and Griffond & Casalis (2000, 2001) have applied the LNP approach to injection-driven fluid motions in porous channels and tubes using the planar and axisymmetric steady flow profiles of Taylor (1956) and Culick (1966), respectively. These are used to mimic the bulk gaseous motion in slab and circular-port rocket motors. Corresponding experimental facilities that utilize a cold gas simulation are referred to as VECLA and VALDO. Other related studies include those on parietal vortex shedding and its connection to intrinsic instability by Lupoglazoff & Vuillot (1996), Couton, Doan-Kim & Vuillot (1997), Ugurtas *et al.* (1999) and Avalon, Casalis & Griffond (1998). The destabilizing effects of headwall injection are also considered by Abu-Irshaid, Majdalani & Casalis (2007) in modelling cylindrically shaped solid and hybrid rocket chambers.

To overcome the limitations of the LNP approach in relation to the problem in cylindrical, axisymmetric geometry (e.g. Griffond *et al.* 2000), a biglobal stability approach has been implemented by Chedevergne & Casalis (2005, 2006*a*) and Chedevergne, Casalis & Féraille (2006). Thus by expressing the disturbance amplitude as a function of two spatial coordinates, radial and axial, the biglobal approach is no longer restricted to a purely exponential form in prescribing spatial amplification or attenuation. In consequence, intrinsic instabilities of the mean flow field are succinctly identified as the primary source of pressure fluctuations (Chedevergne *et al.* 2006). According to Chedevergne & Casalis (2006*a*), biglobal instability predictions compare

favourably with live subscale SRM measurements obtained by Prévost & Godon (2005). They also agree satisfactorily with the large collection of data acquired through VALDO, the cold gas experimental facility operated by Avalon & Josset (2006). In particular, the unstable frequencies reported in the experiments are found to match the circular frequencies recovered from the biglobal stability analysis. Moreover, the biglobal theory is proved to be quite accurate in delineating the frequency paths arising in actual SRMs.

In the present article, some unresolved issues in previous studies are clarified through the use of direct numerical simulation (DNS) investigations. For example, DNS results will be used to: (*a*) verify the dependence of the temporal growth rate on the domain size; (*b*) reproduce the same frequencies and growth rates predicted by the stability eigensolver; and (*c*) confirm the nonlinear coupling between stability eigenmodes and acoustic modes, a mechanism that leads to the emergence of secondary eigenmodes in the flow. Additionally, the oscillatory velocity components obtained through DNS will be shown to match the corresponding stability eigenfunctions when properly augmented by the vorticoacoustic solution of Majdalani & Van Moorhem (1998), and a properly modelled viscous dissipation function that must be applied to the inviscid acoustic amplitudes.

The paper is organized as follows. Before exploring the details of the direct numerical simulation, the first part will be devoted to the biglobal stability equations used to capture the intrinsic instabilities of the flow field. In the process, the unresolved issues of this approach will be pointed out. Next, the procedure used to set up the DNS computations will be described along with the steps needed to evaluate the steady-state motion. This is followed by an overview of the theoretical techniques leading to the assessment of unsteady flow disturbances, including both hydrodynamic instability eigenmodes and pressure-driven vorticoacoustic modes. Our theoretical predictions will be thoroughly verified through comparisons to DNS data obtained using both a static and a dynamic chamber configuration in which the injection velocity at the sidewall is permitted to vary with time. The latter will enable us to continuously change the eigenmode frequency until crossing with the chamber's fundamental acoustic mode occurs. At the outset, the effect of acoustic and hydrodynamic modal crossing will be captured and discussed.

2. Problem configuration

2.1. *Equations of motion*

The configuration used to represent the flow inside a simulated SRM is delineated by a solid boundary at the headwall and a porous, semi-infinite cylindrical surface of radius R that we call the sidewall. Furthermore, we assume that a non-reactive, cold gas is injected uniformly and perpendicularly to the sidewall at a characteristic speed of V_{inj} as illustrated in figure 1. The regression of the propellant grain during rocket firing is modelled by the time evolution of R and V_{inj}.

For a viscous and incompressible fluid, the velocity $\boldsymbol{U} = (U_r, U_\theta, U_x)$ and pressure P satisfy the standard Navier–Stokes equations:

$$\begin{cases} \dfrac{\partial \rho}{\partial t} + \boldsymbol{\nabla} \cdot (\rho \boldsymbol{U}) = 0, \\ \rho \left(\dfrac{\partial \boldsymbol{U}}{\partial t} + \boldsymbol{U} \cdot \boldsymbol{\nabla} \boldsymbol{U} \right) + \boldsymbol{\nabla} P = \mu \Delta \boldsymbol{U}, \end{cases} \tag{2.1}$$

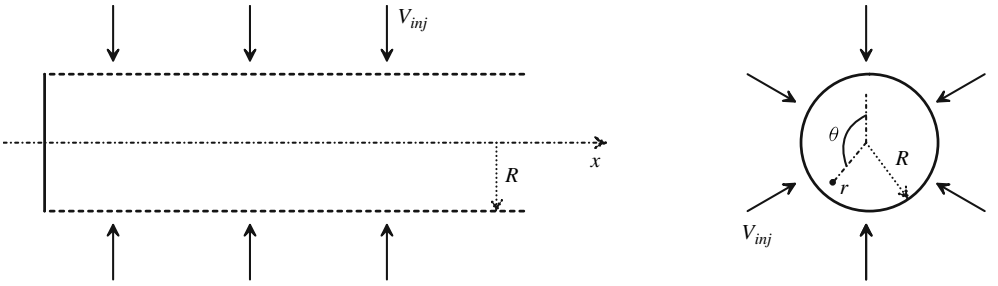

FIGURE 1. Cylindrical coordinate system (r, θ, x). The gas is normally injected through the circumferential wall located at $r = R$ with an inward radial speed equal to V_{inj}. The porous cylinder is bounded by a solid wall located at $x = 0$.

where ρ denotes the flow density and μ the dynamic viscosity. Several boundary conditions may be associated with (2.1), and these correspond to the uniform wall-normal injection, the no-slip condition at the headwall, and the no-divergence condition along the axis $r = 0$:

$$\begin{cases} \forall x, \theta, t \quad U_r(x, R, \theta, t) = -V_{inj} \quad U_\theta(x, R, \theta, t) = U_x(x, R, \theta, t) = 0, \\ \forall r, \theta, t \quad U_r(0, r, \theta, t) = U_\theta(0, r, \theta, t) = U_x(0, r, \theta, t) = 0, \\ \forall x, \theta, t \quad \|\boldsymbol{U}(x, 0, \theta, t)\|, |P(x, 0, \theta, t)| \text{ bounded.} \end{cases} \tag{2.2}$$

Note that a singular point appears at the corner of the domain $(x = 0, r = R)$ where the radial flow entering the chamber from the sidewall is unable to observe the no-slip condition at the headwall. This situation is extensively analysed by Kurdyumov (2008) and will be revisited in § 2.2.2.

The present work is based on a perturbation concept that considers the instantaneous flow field as being composed of a basic, mean flow component and of two types of unsteady fluctuations. While the first type of disturbances is driven by the hydrodynamic instability eigenmodes, the second is due to the acoustic modes in the chamber. For this reason, the evaluation of the basic flow will be examined before analysing the unsteady contributions.

2.2. *Mean flow evaluation*

The classical representation of the mean flow $(\bar{\boldsymbol{U}})$ in a simulated SRM is based on the assumption that the motion may be decomposed into a series of steady-state profiles. As shown by Majdalani, Vyas & Flandro (2002, 2009), the effects of time-dependent propellant grain regression on the mean flow may be safely dismissed in the context of linear stability and vorticoacoustic wave analysis. The characteristic frequencies of these unsteady effects are sufficiently low compared with other flow disturbances to justify ignoring them. Consequently, the radius R and injection velocity V_{inj} may be taken as quasi-steady, even when their values must be updated with each time step based on data acquired from live rocket firings. Moreover, the analysis of Majdalani (2007) suggests that compressibility effects in typical SRMs are only important in chambers with lengths that exceed approximately 40 % of the critical distance needed for the flow to reach choking conditions in the absence of a converging–diverging nozzle.

Hence, by assuming incompressible and axisymmetric mean flow conditions, the system given by (2.1)–(2.2) can be made dimensionless, and written in terms of the

mean flow streamfunction Ψ and the dimensionless vorticity $\bar{\boldsymbol{\Omega}} = \bar{\Omega}\boldsymbol{e}_\theta = \boldsymbol{\nabla} \times \bar{\boldsymbol{U}}$. In this process, spatial coordinates, time, velocity components and pressure are normalized using R, R/V_{inj}, V_{inj} and ρV_{inj}^2, respectively. These render

$$\begin{cases} \bar{\Omega} = -\mathscr{L}\Psi = -\left(\dfrac{\partial^2\Psi}{\partial x^2} + \dfrac{\partial^2\Psi}{\partial r^2} - \dfrac{1}{r}\dfrac{\partial\Psi}{\partial r}\right), \\ \dfrac{\partial\Psi}{\partial r}\dfrac{\partial(\bar{\Omega}/r)}{\partial x} - \dfrac{\partial\Psi}{\partial r}\dfrac{\partial(\bar{\Omega}/r)}{\partial x} + \dfrac{1}{Re}\left(\dfrac{\partial^2\bar{\Omega}}{\partial x^2} + \dfrac{\partial^2\bar{\Omega}}{\partial r^2} + \dfrac{1}{r}\dfrac{\partial\bar{\Omega}}{\partial r} - \dfrac{\bar{\Omega}}{r}\right) = 0, \end{cases} \tag{2.3}$$

where the Reynolds number $Re = \rho R V_{inj}/\mu$ depends on the instantaneous radius and injection velocity. The linear operator $\mathscr{L} = \partial^2/\partial x^2 + \partial^2/\partial r^2 - r^{-1}\partial/\partial r$ connecting the mean flow vorticity and the streamfunction is used later to define the linear stability problem in (3.2). At this stage, the physical conditions stemming from (2.2) may be expressed in terms of Ψ and written as

$$\begin{cases} \forall x : \dfrac{\partial\Psi}{\partial r}(x,1) = 0, \quad \dfrac{\partial\Psi}{\partial x}(x,1) = 1, \\ \forall r : \dfrac{\partial\Psi}{\partial r}(0,r) = \dfrac{\partial\Psi}{\partial x}(0,r) = 0, \\ \forall x : \dfrac{\partial^3\Psi}{\partial r^3}(x,0) = \dfrac{\partial\Psi}{\partial r}(x,0) = \dfrac{\partial\Psi}{\partial x}(x,0) = 0. \end{cases} \tag{2.4}$$

Note that the last three relations are deduced from the axisymmetric conditions along $r = 0$, namely, $\bar{U}_r = 0$ and $\partial\bar{U}_x/\partial r = 0$. They can also be derived from (2.3) after expanding Ψ in a Taylor series about $r = 0$.

2.2.1. *Taylor–Culick motion*

Similarity solutions for (2.3)–(2.4) exist provided that the corner condition that requires forcing $\bar{U}_r = 0$ at $x = 0$ is relaxed. In the absence of this singularity, one may follow Berman (1953) and posit $\Psi = xF(r)$ to the extent of retrieving

$$\begin{cases} \left[\left(\dfrac{F}{r}\right)\left(\dfrac{F'}{r}\right)' - \left(\dfrac{F'}{r}\right)^2\right]' + \dfrac{1}{Re}\left[\dfrac{1}{r}\left(r\left(\dfrac{F'}{r}\right)'\right)'\right]' = 0, \\ \lim\limits_{r\to 0}(F'' - F'/r)/r = F(0) = F'(1) = 0, \quad F(1) = 1, \end{cases} \tag{2.5}$$

where primes denote differentiation with respect to r. As shown independently by Taylor (1956) and Culick (1966), an exact solution of (2.5) exists for an infinite Reynolds number, with $\bar{\Omega} = C^2 r\Psi$ and $C \in \mathbb{R}$. The corresponding Taylor–Culick motion is defined by

$$\begin{cases} \bar{U}_r = -\dfrac{1}{r}\sin\left(\dfrac{1}{2}\pi r^2\right) \\ \bar{U}_x = \pi x\cos\left(\dfrac{1}{2}\pi r^2\right) \end{cases} \quad \bar{P} = -\frac{\pi^2 x^2}{2} - \frac{1}{2r^2}\sin^2\left(\frac{1}{2}\pi r^2\right) + P_0 \tag{2.6}$$

where P_0 is the reference pressure at the headwall centre.

To illustrate the non-parallel nature of the Taylor–Culick flow due to radial injection at $r = 1$, analytical streamlines are depicted as solid lines in figure 2. We also note that the motion becomes gradually more parallel in the downstream direction, away from the headwall.

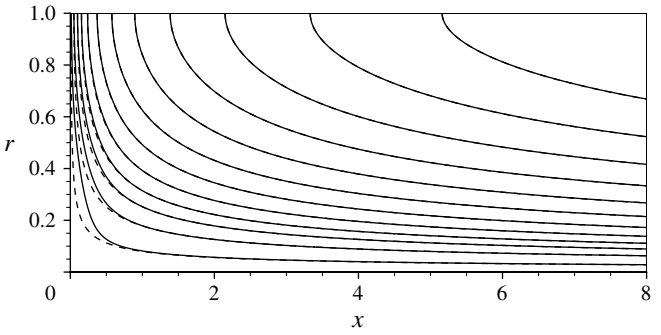

FIGURE 2. Streamlines of the mean flow solutions. Solid lines correspond to the DNS-computed base flow used in § 4, whereas dashed lines stand for the Taylor–Culick analytical solution given by (2.6).

In studying the influence of the mean flow on one-dimensional linear stability, Griffond *et al.* (2000) show that (2.6) represents a legitimate solution of Berman's equation for $Re > 1000$. Furthermore, Majdalani & Akiki (2010) show that viscous effects do not play any appreciable role in modifying the flow characteristics, especially when the no-slip condition $\bar{U}_r(0, r) = 0$ is discounted. These theoretical predictions are corroborated by the excellent agreement between the Taylor–Culick profile and cold-flow measurements acquired by Avalon & Josset (2006) using an experimental facility known as VALDO. The latter has a radius of $R_0 = 0.03$ m and allows V_{inj} to vary from 0.6 m s^{-1} up to 2 m s^{-1}, thus permitting its Reynolds number to range between 1200 and 4000. In this setup, a fluid is injected across a porous cylinder that is made of poral, a permeable bronze metal. In addition to these in-house experiments, the Taylor–Culick motion is actually confirmed through a set of laboratory investigations carried out by Dunlap *et al.* (1990). In both experiments, it is reported that agreement with experimental data is maintained as long as the flow remains laminar with $x/R < 12$. It can thus be seen that the inviscid Taylor–Culick solution provides an excellent approximation of the Berman equation for large Re and $x/R < 12$.

2.2.2. *Computed mean flows*

In seeking a more accurate representation of the mean flow, a numerically computed solution will be needed, particularly one that remains valid both in the headwall region and far downstream. To overcome the inconsistency at the point (0, 1), a simple idea may be borrowed from the cold-flow apparatus VALDO and then implemented into our model by introducing a spatially varying velocity distribution $V_{inj}(x)$ along the sidewall. This spatial function will satisfy the condition $V_{inj}(0) = 0$ while still permitting a smooth C^2 transition to the final value of $V_{inj} = 1$, after crossing a designated distance from headwall that we refer to as x_{link}. Different feasible test functions have in fact been explored and these are summarized in a paper by Chedevergne & Casalis (2006*b*).

To start with, the computation of the mean flow is performed for a porous cylinder truncated at $x = X_e$ using a multi-module, multi-physics code named CEDRE. This solver is developed at ONERA with the objective of serving multiple functions and flow regimes, including instantaneous velocity and pressure calculations in a user-defined SRM chamber. Spatial discretization in CEDRE is based on a finite volume

Δr_{min}	Δr_{max}	Δx_{min}	Δx_{max}
2.89×10^{-6} m	2.945×10^{-4} m	2.29×10^{-6} m	1.2566×10^{-3} m

TABLE 1. Grid spacings used to compute both mean and unsteady flows.

approach that employs an upwind Roe scheme with a second-order extension (MUSCL scheme with Van Leer limiter). A complete description of the code is given by Refloch *et al.* (2011) and more specific information concerning code validation for rocket simulations may be gleaned from a survey by Vuillot, Scherrer & Habiballah (2003).

In the interest of establishing realistic baseline cases, the characteristic length and velocity are chosen to match those employed in the VALDO facility by Avalon & Josset (2006). For this reason, we use a chamber radius of $R = R_0 = 0.03$ m and an injection velocity of $V_{inj} = 1$ m s^{-1}. Homogeneous boundary conditions are subsequently used, corresponding to the velocity adherence at $x = 0$, the constant normal velocity injection at $r = R$, and symmetry conditions at $r = 0$. At $x = X_e$, a radial pressure equilibrium is imposed so that the average pressure is equal to P_{atm}:

$$\frac{1}{R}\int_0^R P(\boldsymbol{r})\,\mathrm{d}\boldsymbol{r} = P_{atm}. \tag{2.7}$$

Four meshes are successively tested to the extent of establishing grid independence. Our sample results for $X_e = 8$ are performed with a Cartesian grid that is composed of 301×161 nodes (later, for $X_e = 10$, the grid is increased to 351×161 nodes such that the thickness of the cells at the headwall remains identical to the $X_e = 8$ case). Furthermore, cosine repartition is employed such that the thickness of the cells on the boundaries is suitably refined close to the headwall. The minimum and maximum grid spacings used are given in table 1.

Here, calculations are conducted in the (x, r) plane assuming an axisymmetric, rotational, laminar flow. To reach steady state, an implicit time scheme is used with a fixed value of the Courant–Friedrichs–Lewy (CFL) number. Using CFL $= 10$, steady-state runs are performed to obtain the basic flow components whose (dashed) streamlines are depicted in figure 2. Compared to the Taylor–Culick approximation, one may infer that good agreement exists. Both solid and dashed lines merge quite rapidly as one departs from the headwall. The limiting case of $x_{link} = 0$ with $V_{inj} =$ const. (which proves to be mesh-dependent) differs from the Taylor–Culick solution solely because of the viscous effects that are neglected in the analytical model expressed through (2.6).

Figure 3(*a,b*) provides views of the mean axial and radial velocity components computed at a dimensionless $X_e = 8$ and $V_{inj} = 1$ m s^{-1}. It is clear that this flow closely resembles the Taylor–Culick model except in the front-end region, where a boundary layer develops. The agreement obtained between the computed flow and the Taylor–Culick profile confirms the essentially incompressible character of this motion. While a compressible solution for the Taylor–Culick problem has been recently developed by Majdalani (2007), it is not considered here due to the relatively small velocities characterizing our problem.

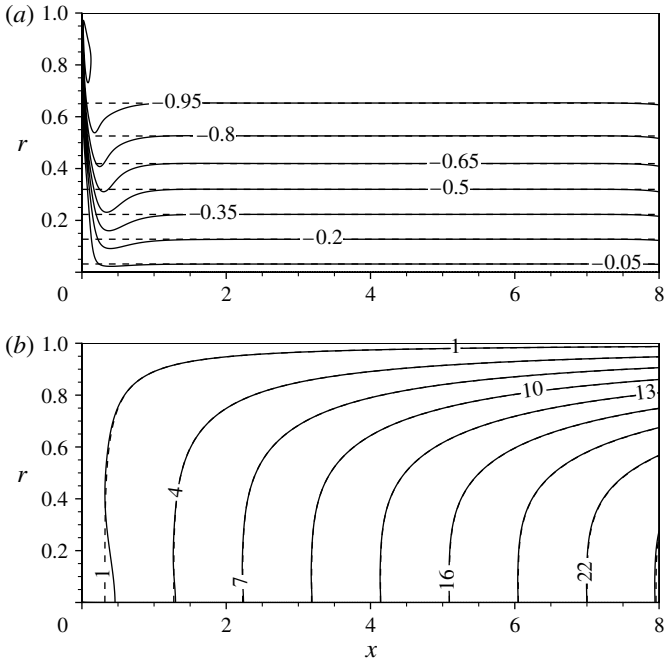

FIGURE 3. Contour lines of the axial and radial components of the basic flow velocity: (*a*) $\bar{U}_x$ and (*b*) $\bar{U}_r$. Solid lines represent the DNS-computed mean flow and dashed lines display the analytical solution given by (2.6).

At this stage, it may be instructive to note that, as described in detail by Chedevergne & Casalis (2006*b*), the impact of a numerically acquired mean flow on hydrodynamic instability eigenmodes may be shown to be weak in the extent of small x_{link} values. On the one hand, although the physical nature of the eigenmodes remains indifferent to the choice of analytical or computed motions, using a computed mean flow leads to a more accurate specification of the eigenvalues. For this reason, the computed field will be used in the stability analysis. On the other hand, unlike hydrodynamic stability eigenmodes, acoustic modes remain unaffected by the small mean flow differences that arise in the front-end region. This may be attributed to the markedly longer wavelengths associated with acoustic oscillations. The attendant behaviour will be illustrated in § 3.2, where the limited impact of the mean flow approximation on the acoustic modes will be discussed. Unless noted otherwise, the analytical Taylor–Culick profile will be the basis of the vorticoacoustic wave analysis.

In what follows, the term 'mean flow' will designate the steady-state solution obtained either numerically or analytically, depending on whether the analysis refers to hydrodynamic stability or acoustic mode calculations, respectively.

3. Theoretical treatment of flow disturbances

When a basic flow is perturbed, it gives rise to both incompressible, hydrodynamic instability eigenmodes, and to compressible, pressure-driven acoustic modes. The corresponding disturbances may be determined using techniques based on biglobal instability, Helmholtz wave decomposition, and small perturbation theories. In this

study, only a brief overview of the relevant theories will be presented. Substantially more detailed descriptions can be found in work by Chedevergne *et al.* (2006) and Majdalani (2009).

3.1. *Hydrodynamic instability eigenmodes*

3.1.1. *Streamfunction formulation*

Eigenmodes of the flow induced by wall-normal injection originate in accordance with biglobal stability theory. In fact, a biglobal approach is needed because of the non-parallel nature of the basic flow, especially for small x. The linear theory that we rely on is based on a perturbation notion that considers any physical quantity Q to be a superposition of a mean variable $\bar{Q}$ and a fluctuating, time-dependent part q. The decomposition $Q = \bar{Q} + q$ can be introduced into the Navier–Stokes equations which, after some simplifications and cancellations, give rise to a linear system of partial differential equations (PDEs). These PDEs prescribe the motion of time-dependent disturbances q. Because of linearity, only one-way coupling is permitted such that the mean flow can affect the disturbances but not the other way around. In the linearized system of equations, the Reynolds number Re, the mean flow $\bar{Q}$, and its various derivatives, define the main coefficients. Accordingly, any perturbation q may be judiciously expressed as

$$q = \hat{q}(x, r)\mathrm{e}^{\mathrm{i}(n\theta - \omega t)}, \quad n \in \mathbb{N}, \ \omega \in \mathbb{C}. \tag{3.1}$$

This unsteady variable representation is mathematically consistent with the mean flow being dependent on both x and r. It can thus be seen that biglobal theory differs from the local stability concept where the amplitude function $\hat{q} = \hat{q}(r)$ is strictly one-dimensional. In (3.1), n is an integer that denotes the azimuthal wavenumber (an index that vanishes for purely axisymmetric disturbances), θ stands for the azimuthal angle, and ω represents the complex circular frequency. While its real part ω_r reproduces the circular frequency of oscillations, its imaginary part ω_i controls the temporal growth rate.

Based on the findings of Chedevergne & Casalis (2005, 2006*a*) and the supporting experimental measurements gathered from subscale SRMs by Prévost & Godon (2005), the hypothesis of axisymmetric disturbances seems quite appropriate as it leads to near-perfect agreement between theory and measurements. Furthermore, by focusing on the $n = 0$ eigenmodes, a two-dimensional streamfunction ψ may be introduced to capture the essence of the disturbances. This simplification enables us to reduce the linearized Navier–Stokes equations into a single, fourth-order PDE written for the unsteady streamfunction $\psi(x, r) = \hat{\psi}(x, r)\mathrm{e}^{\mathrm{i}(n\theta - \omega t)}$. We get

$$\begin{aligned} &\frac{1}{r}\frac{\partial \Psi}{\partial r}\frac{\partial(\mathscr{L}\hat{\psi})}{\partial x} - r\frac{\partial \Psi}{\partial x}\frac{\partial}{\partial r}\left(\frac{1}{r^2}\mathscr{L}\hat{\psi}\right) + \frac{\partial \hat{\psi}}{\partial r}\frac{\partial}{\partial r}\left[\frac{1}{r}\frac{\partial}{\partial r}\left(\frac{\partial \Psi}{\partial x}\right)\right] \\ &\quad - r\frac{\partial \hat{\psi}}{\partial x}\frac{\partial}{\partial r}\left[\frac{1}{r}\frac{\partial}{\partial r}\left(\frac{1}{r}\frac{\partial \Psi}{\partial r}\right)\right] - \frac{1}{Re}\mathscr{L}(\mathscr{L}\hat{\psi}) = \mathrm{i}\omega\mathscr{L}\hat{\psi}. \end{aligned} \tag{3.2}$$

At this point, one may recall that the instantaneous flow $Q = \bar{Q} + q$ must satisfy the original boundary conditions stipulated in (2.4). This permits deducing the assortment

of conditions that must be imposed on $\hat{\psi}$, namely,

$$\begin{cases} \forall x : \dfrac{\partial \hat{\psi}}{\partial r}(1,x) = 0; \quad \dfrac{\partial \hat{\psi}}{\partial x}(1,x) = 0, \\ \forall r : \dfrac{\partial \hat{\psi}}{\partial r}(r,0) = \dfrac{\partial \hat{\psi}}{\partial x}(r,0) = 0, \\ \forall x : \dfrac{\partial^3 \hat{\psi}}{\partial r^3}(r,0) = \dfrac{\partial \hat{\psi}}{\partial r}(r,0) = \dfrac{\partial \hat{\psi}}{\partial x}(r,0) = 0. \end{cases} \tag{3.3}$$

Next, we sketch the numerical scheme that must be applied to (3.2)–(3.3).

3.1.2. *Numerical procedure*

Equation (3.2) can be solved directly for $(x, r) \in [0, X_e] \times [0, 1]$ provided that a suitable outflow condition is made available at $x = X_e$. We follow Theofilis (2003, 2011), Theofilis, Duck & Owen (2004) and Casalis *et al.* (2004), who utilize a simple linear extrapolation relation. Thus, given a number of discretization points N_x in the streamwise direction, we set, for all r:

$$\hat{\psi}(X_e, r) = \hat{\psi}(X_{N_x}, r) = \frac{X_{N_x} - X_{N_x-2}}{X_{N_x-1} - X_{N_x-2}} \hat{\psi}(X_{N_x-1}, r) + \frac{X_{N_x-1} - X_{N_x}}{X_{N_x-1} - X_{N_x-2}} \hat{\psi}(X_{N_x-2}, r). \tag{3.4}$$

Discretization of the computational domain $[0, X_e] \times [0, 1]$ may be effected using Chebyshev polynomials. After some effort, (3.2)–(3.4) are turned into a generalized eigenvalue problem of the form $\mathscr{A}\psi = \omega\mathscr{B}\psi$. Here the unknown eigenvector ψ refers to an arrangement of the discretized values of $\hat{\psi}(x, r)$ whereas ω corresponds to one of the (unknown) eigenvalues. Finally, Arnoldi's algorithm may be implemented to produce the problem's complex eigenvalues, ω, and their associated eigenvectors ψ, as shown for example by Golub & Loan (1996).

3.1.3. *Biglobal stability spectra*

As alluded to earlier, the stability results featured in this work are based on a numerically computed mean flow. Two sample sets of complex eigenvalues are showcased in figure 4 for $Re = 1975$ and $X_e = 8$ and 10. Interestingly, although the spectra appear at approximately the same circular frequencies, their temporal growth rates increase with the chamber length. Everywhere, the CEDRE-computed basic flow corresponds to $R = 0.03$ m and $V_{inj} = 1$ m s^{-1}.

For each eigenvalue ω, a companion eigenvector ψ may be retrieved, thus leading to the recovery of the axial and radial velocity eigenfunctions $\hat{u}_x$ and $\hat{u}_r$ directly from

$$\hat{u}_x = \frac{1}{r}\frac{\partial \hat{\psi}}{\partial r} \quad \text{and} \quad \hat{u}_r = -\frac{1}{r}\frac{\partial \hat{\psi}}{\partial x}. \tag{3.5}$$

Clearly, any disturbance $q = \hat{q}\mathrm{e}^{-\mathrm{i}\omega t}$, determined by its eigenvalue ω, contains the essential fluctuating flow ingredients such as u_x, u_r, p and their derivatives. Using the constant parameters R and V_{inj}, the complete set of perturbations q may be transformed into dimensional quantities. Although mathematically q can be complex, the associated physical perturbation is given by its real part $\mathrm{Re}(q)$. Then, given an

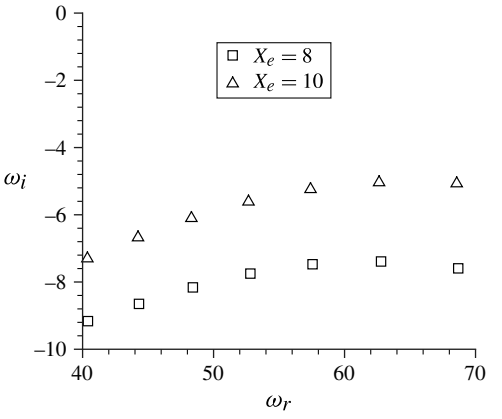

FIGURE 4. Set of eigenvalues in the complex (ω_r, ω_i) plane for $Re = 1975$. Two cases are shown: $X_e = 8$ (squares) and $X_e = 10$ (triangles).

eigenmode $\omega = \omega^0$, the ensuing physical disturbance may be deduced from

$$\begin{cases} \mathrm{Re}(A\hat{q}\,\mathrm{e}^{-\mathrm{i}(V_{inj}/R)\omega^0 t}) = A[(\hat{q})_r \cos(2\pi ft) + (\hat{q})_i \sin(2\pi ft)]\,\mathrm{e}^{\nu t}, \\ \text{with} \quad f = \dfrac{V_{inj}}{2\pi R}\omega_r^0 \quad \text{and} \quad \nu = \dfrac{V_{inj}}{R}\omega_i^0 \end{cases} \tag{3.6}$$

where $\omega^0 = \omega_r^0 + \mathrm{i}\omega_i^0$ and A represents the initial amplitude of the perturbation, an initially unknown value. Naturally, it is not necessary to specify A because q is a solution to a linear system.

Two major results stemming from the stability analysis can be immediately pointed out. First, we note that the spectrum in figure 4 is discrete. As such, only a discrete set of dimensionless frequencies ω_r exists for which disturbances may develop from the mean flow. Second, all of the eigenvalues ω bear a negative imaginary part. This implies that all of the eigenmodes will be exponentially damped in time. However, their associated eigenfunctions will grow exponentially in the streamwise direction, as illustrated in figure 5(*a,b*). These three-dimensional surface plots display the spatial evolution of the real part of the eigenfunctions $\hat{u}_x$ and $\hat{u}_r$ for the eigenvalue $\omega^0 = 40.409 - 9.164\mathrm{i}$ and $X_e = 8$. Without having been explicitly prescribed in the formulation of the disturbance itself, as in (3.1), the axial fluctuation in figure 5(*a*) points to the existence of a strong (exponential-like) amplification in the x direction. The spatial amplification is thus implicitly embedded in the biglobal stability framework.

We conclude that, for a given eigenvalue, two counteracting mechanisms are seen to coexist: a temporal decay affecting the perturbations as time elapses and a spatial growth in the perturbed amplitudes as the wave propagates downstream. These eigenmodes do not represent absolute instabilities. Provided that X_e remains small in figure 4, the flow will continue to be globally stable. The influence of X_e on the eigenvalues will be further discussed in § 4.

3.2. *Vorticoacoustic modes*

In the absence of mean flow instability, the flow driven by wall-normal injection in a porous chamber is strongly susceptible to vorticoacoustic oscillations. These are

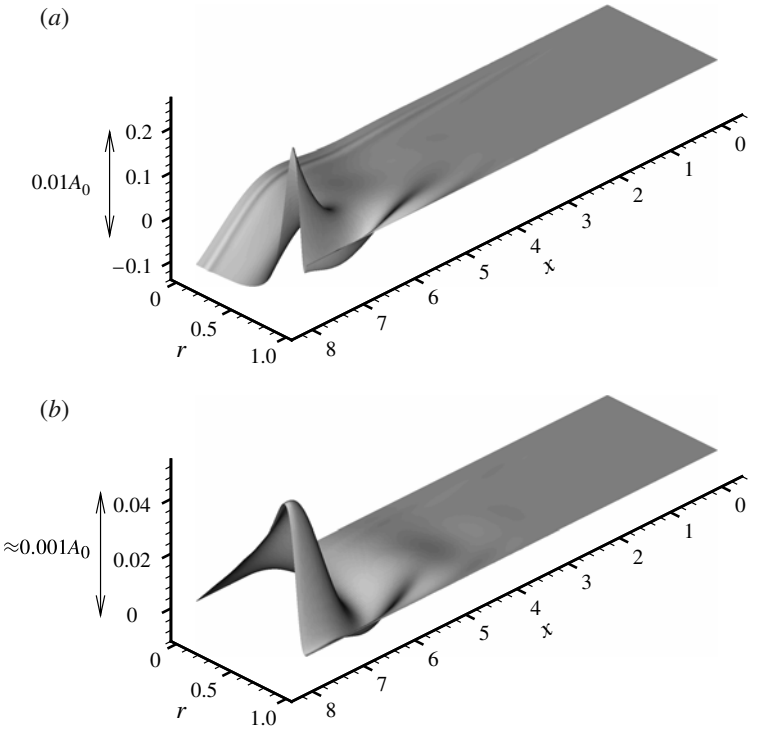

FIGURE 5. Axial and radial components of the velocity eigenfunctions (real parts) for eigenmode $\omega = 40.409 - 9.164\mathrm{i}$: (*a*) $\hat{u}_x$ and (*b*) $\hat{u}_r$. Here $t = 0$ and the initial amplitude in (3.6) is taken as $A = 0.01A_0$, where A_0 is defined in figure 3(*a*).

invariably reported in SRM chambers due to small, inevitable fluctuations in the injection process (Majdalani, Flandro & Roh 2000). Unlike hydrodynamic instability disturbances, which evolve over short wavelengths and characteristic speeds at the order of the mean flow, the vorticoacoustic waves travel over much longer wavelengths and a much higher speed, namely, that of sound. The disparity in spatial and temporal scales over which these two types of disturbances propagate enables us to linearly superimpose their contributions and obtain the total unsteady fluctuation in the chamber.

With the instability eigenfunctions already in hand, the vorticoacoustic waves remain to be determined, and these have been systematically investigated by Majdalani and co-workers in a variety of geometries and flow configurations (see, for example, Majdalani & Van Moorhem 1998; Majdalani 1999; Majdalani & Roh 2000; Majdalani 2001*a*,*b*; Majdalani & Flandro 2002; Majdalani 2009). Unlike the instability waves, which cannot be obtained except by computer, the vorticoacoustic framework leads to closed-form approximations that can be used to directly describe the oscillatory waves driven by pressure fluctuations. In what follows, only the basics of Majdalani's approach will be revisited.

In the analytical framework, a small perturbation q is superimposed on the mean flow $\bar{Q}$ to the extent of linearizing the compressible Navier–Stokes equations before seeking an asymptotic solution. The steady motion $\bar{Q}$ may be equated to the Taylor–Culick profile, although the time-dependent formulation has been

generalized to the extent of accommodating an arbitrary mean flow (see Majdalani 2001*a*; Majdalani & Flandro 2002; Majdalani 2009). Subsequently, the Helmholtz decomposition theorem can be used to split the temporal perturbation q into two complementary parts: $q = \breve{q} + \tilde{q}$. Here $\breve{q}$ defines the irrotational compressible wave, which is pressure-driven, and $\tilde{q}$ denotes the incompressible rotational part, which is induced by unsteady vorticity originating at the boundaries. Chu & Kovásznay (1958) refer to these fluctuations as mass-like or force-like, sound or vorticity disturbance modes, respectively. In the present configuration, $\breve{q}$ stands for the irrotational acoustic wave, which is dominated by longitudinal oscillations in a porous cylinder with no flow, thus leaving $\tilde{q}$ to serve as the correction needed to account for the basic flow pattern $\bar{Q}$. As noted by Griffond (2002), $\tilde{q}$ controls the vorticoacoustic boundary layer and this component has been resolved using several perturbation methods such as multiple scales and WKB.

For an axisymmetric cylinder, the sound wave $\breve{q}$ may be expressed as

$$\begin{cases} \breve{p}(x, t^*) = \cos(\omega_m x)\mathrm{e}^{-\mathrm{i}\omega_m t^*}, \\ \breve{\boldsymbol{u}}(x, t^*) = \mathrm{i}\sin(\omega_m x)\mathrm{e}^{-\mathrm{i}\omega_m t^*}\boldsymbol{e}_x \end{cases} \tag{3.7}$$

where $\breve{p}$ and $\breve{\boldsymbol{u}}$ are the pressure and velocity fluctuations of the longitudinal plane wave. Using a_0 for the speed of sound, these fluctuations are normalized by a characteristic time $t^* = ta_0/R$, which captures the time that an acoustic disturbance consumes while crossing the radius. For the closed–open acoustic conditions imposed by the present configuration, one may use a circular frequency of $\omega_m = (m - \frac{1}{2})\pi/X_e$, where $m \in \mathbb{N}^*$.

As shown by Majdalani & Flandro (2002), the boundary-driven vorticity wave $\tilde{q}$ associated with a steady motion $\bar{Q}$ can be expressed in terms of a self-similar mean flow streamfunction, $\Psi(x, r) = xF(r)$. By letting $\tilde{q}$ designate the velocity fluctuation $\tilde{u}$, we have

$$\begin{cases} \tilde{u}_x = -\mathrm{i}\left(\dfrac{F}{F_0}\right)\mathrm{e}^{[\zeta - \mathrm{i}(\omega_m t^* + \Phi)]}, \quad F_0 \equiv F(1), \quad F_0' \equiv F'(1), \\ \tilde{u}_r = -\dfrac{M}{r}\left(\dfrac{F}{F_0}\right)^3 \mathrm{e}^{[\zeta - \mathrm{i}(\omega_m t^* + \Phi)]}, \end{cases} \tag{3.8}$$

where $M = V_{inj}/a_0$ is the wall injection Mach number. Using the generalized-scaling technique introduced by Majdalani & Rienstra (2002), $\zeta(r)$ and $\Phi(r)$ may be written at order Re^{-1},

$$\begin{cases} \zeta(r) = \xi \displaystyle\int_1^r x^3 F^{-3}(x)\,\mathrm{d}x, \\ \Phi = S_m \left[\displaystyle\int_1^r (xF^{-1} - 4Re^{-1}xF^{-2}) + \frac{3}{2}Re^{-1}(r^2F^{-2} - F_0^{-2})\right], \end{cases} \tag{3.9}$$

where

$$\xi = \frac{S_m^2}{Re} = \frac{\omega_m^2}{M^2 Re}, \quad S_m = \frac{\omega_m}{M}, \quad Re = \frac{V_{inj}R}{\nu}, \tag{3.10}$$

and the characteristic function F may be taken to be

$$F(r) = \begin{cases} r^2(2 - r^2) & 10 < Re < 100, \\ \sin(\frac{1}{2}\pi r^2) & Re \geqslant 100. \end{cases} \tag{3.11}$$

The Taylor–Culick flow becomes a special case for which $F = \sin\theta$, $F_0 = 1$, $F_0' = 0$, and $\theta = \frac{1}{2}\pi r^2$. The corresponding solution reduces to

$$\begin{cases} \tilde{u}_x = -\mathrm{i}\sin\theta\,\sin\left(\omega_m x\sin\theta\right)\mathrm{e}^{[\zeta-\mathrm{i}(\omega_m t^*+\Phi)]}, \\ \tilde{u}_r = -\dfrac{M}{r}\sin^3\theta\cos(\omega_m x\sin\theta)\mathrm{e}^{[\zeta-\mathrm{i}(\omega_m t^*+\Phi)]}, \\ \zeta = -\dfrac{\xi}{\pi^2}\left[\csc\theta - 1 + \theta\cot\theta\csc\theta + I\left(\dfrac{1}{2}\pi\right) - I(\theta)\right], \\ \Phi = \dfrac{S_m}{\pi}\ln\tan\left(\dfrac{1}{2}\theta\right) + \dfrac{S_m}{\pi Re}\left[4\cot\theta + 3\left(\theta\csc^2\theta - \dfrac{1}{2}\pi\right)\right], \\ I(\theta) = \theta + 2\displaystyle\sum_{k=1}^{\infty}\frac{\left(1-2^{1-2k}\right)}{(2k+1)\pi^{2k}}\left(\sum_{j-1}^{\infty}\frac{1}{j^{2k}}\right)\theta^{2k+1} \\ \qquad = \theta + \dfrac{1}{18}\theta^3 + \dfrac{7}{1800}\theta^5 + \dfrac{31}{105840}\theta^7 + \cdots. \end{cases} \tag{3.12}$$

A simpler closed-form expression may be obtained, as shown by Majdalani & Van Moorhem (1998), using the concept of composite scales. The so-called 'CST' technique is a variant of multiple scales theory and applies to the treatment of some problems with nonlinear scales (see Majdalani 1998, 2001*a*). At the outset, one may employ a practically equivalent expression to (3.12), namely,

$$\begin{cases} \zeta = -\xi\left[\dfrac{\eta(r)r^3}{F^3} - \dfrac{\eta(1)}{F_0^3}\right] = -\xi\dfrac{\eta(r)r^3}{\sin^3\theta}, \\ \eta(r) = \dfrac{1-r}{1+\dfrac{3}{2}(1-r)^{3/2}\left(\dfrac{1-r}{r} - \dfrac{3}{2}\ln r\right)}, \\ \Phi = S_m\displaystyle\int_1^r\frac{x}{F}\,\mathrm{d}x + \frac{S_m}{Re}\left[\frac{\eta(r)r}{F^3}(3rF' + 2F) - \frac{\eta(1)}{F_0^3}(3F_0' + 2F_0)\right] \\ \qquad = \dfrac{S_m}{\pi}\ln\tan\left(\dfrac{1}{2}\theta\right) + \dfrac{2S_m}{Re}\dfrac{\eta(r)r}{\sin^2\theta}\left(1 + \dfrac{3\theta}{\tan\theta}\right). \end{cases} \tag{3.13}$$

A detailed characterization of the vorticoacoustic layer that accompanies (3.13) is given by Majdalani (1999). Figure 6 illustrates the distribution of the axial component of the wave by providing four radial profiles along the chamber for the first acoustic mode. The irrotational component $\breve{u}_x$ can be identified as the driver of the rotational part $\tilde{u}_x$. Their combination leads to the vorticoacoustic velocity fluctuation in the axial direction.

The relations formed by (3.7)–(3.13) constitute a practical framework for analytically approximating the acoustic modes while accounting for the effects of the mean flow $\bar{Q}$, especially in the case of the Taylor–Culick profile. When using the latter, the vorticoacoustic approximation will be valid everywhere except in the close vicinity of the headwall. This particular limitation remains secondary because fluctuations near the headwall are so small that they can be of no material consequence.

As for the modal dependence on X_e, it may be helpful to remark that the acoustic frequencies are directly impacted by variations in the chamber length through $\omega_m = (m - \frac{1}{2})\pi/X_e$. So while X_e plays an appreciable role in controlling the frequency

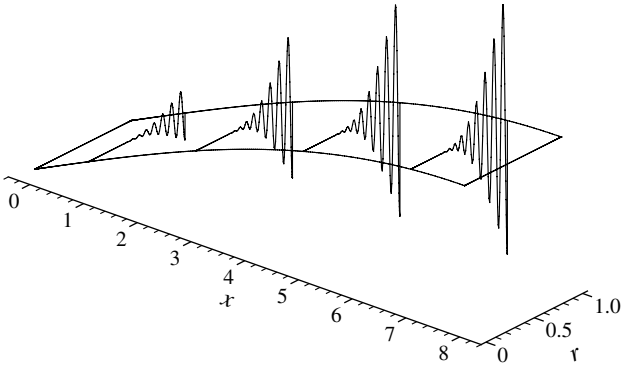

FIGURE 6. Radial profiles of the longitudinal velocity of the first acoustic mode $\omega_1 = 6.545$.

of the compressible mode, its effect on the incompressible eigenmode ω_r remains secondary. This behaviour is corroborated by the spectrum of figure 4, where the influence of X_e on ω_r can hardly be seen.

4. Direct numerical simulation (DNS)

It may be generally hypothesized that amplification of thrust oscillations can be attributed to coupling mechanisms between acoustic modes and hydrodynamic instability frequencies. To investigate such potential interactions, DNS calculations are performed with the aim of elucidating the unsteady wave behaviour. In this effort, two separate types of computations are carried out and these correspond to two distinct configurations. The first aims at investigating the coupling between eigenmode frequencies and acoustic modes in the context of a static configuration in which both R and V_{inj} remain fixed. This setup can also permit characterizing the dependence of biglobal stability eigenmodes on X_e.

In the second set of numerical experiments, which we call dynamic, V_{inj} is varied to the extent of reproducing the emergence of eigenmodes through acoustic forcing.

The DNS computations of the unsteady disturbances represent a continuation to the simulation initiated in § 2.2.2 based on ONERA's code CEDRE. For consistency, the same geometric and input parameters used to obtain the steady-state solution are retained in the unsteady flow investigation.

4.1. *Static cases*

The primary reason behind DNS computations in a static configuration is to isolate the influence of one specific eigenmode on the acoustic field. As stated in § 3.1, an eigenmode can be characterized by its dimensionless frequency ω_r. Depending on the proximity of ω_r to the acoustic frequencies, different outcomes may be expected. In addition, since the dependence of eigenmodes on X_e has been brought into question, several test cases will be simulated with varying chamber lengths.

4.1.1. *Computational strategy*

Our strategy is to superimpose, at the initial time, a representative eigenmode $\omega = \omega^0 = 40.409 - 9.164\mathrm{i}$ (extracted from the spectrum in figure 4), on the DNS-calculated basic flow. The eigenvelocities u_x and u_r associated with ω^0 are projected on the DNS grid and added to the previously computed mean flow. The projection is made so that fluctuations in u_x and u_r follow (3.6) at $t = 0$.

Regarding u_x, we take $A^{u_x} = 0.01A_0$, with A_0 being the peak value attained by the longitudinal component $\bar{U}_x$ as shown in figure 3(*a*). This value is selected so that fluctuations remain in the linear range relative to the mean flow. As for the amplitude factor A^{u_r}, it is prescribed by the stability calculation. Typically, one gets $A^{u_r} \approx 0.1A^{u_x}$. Given that the initial time corresponds to $t = 0$ s, only the real parts $(\hat{u}_x)_r$ and $(\hat{u}_r)_r$ need to be introduced into the simulations.

It may be important to note that the pressure perturbation of the stability mode $\omega = \omega^0$ is not superimposed on the pressure distribution of the mean flow, being very small in amplitude. At first glance, the superposition process may appear to be simple. Actually, the superposition of the mean and unsteady components requires careful grid projections to avoid introducing spurious errors. It also requires special attention to the boundary conditions.

To compute the unsteady field, an explicit time scheme is used with a time step of $\Delta t = 5 \times 10^{-9}$ s. The corresponding maximum CFL number is kept under unity. With the origin of time being set at $t = 0$ s, our computer runs are stopped after 4 000 000 iterations, at $t = 0.02$ s. Subsequently, signals from different virtual sensors (placed to cover the flow in the entire chamber) are extracted and analysed.

It should be remarked that other comparable strategies exist for exploring the character of oscillations in simulated SRMs. For example, Apte & Yang (2001*a*,*b*, 2003) introduce white noise or an acoustic excitation to perform LES calculations that can be quite effective at capturing the triggered instabilities.

4.1.2. *Three representative cases*

Using the strategy described above, several representative computations are performed by changing the eigenmode introduced at $t = 0$ s or the length of the chamber X_e. In what follows, three benchmark cases are chosen at fixed values of R and V_{inj}. The first two enable us to capture the effect of changing X_e. The third one aims at exploring the nonlinear behaviour that emerges from eigenmodes being close to the main chamber's acoustic frequency.

(i) Case 1: introduces $\omega^0 = 40.409 - 9.164\mathrm{i}$ in the DNS code using $X_e = 8$. The corresponding frequency is calculated to be $f = V_{inj}\omega_r^0/(2\pi R_0) = 214$ Hz.

(ii) Case 2: introduces $\omega^0 = 40.367 - 7.302\mathrm{i}$ in the DNS code using $X_e = 10$. Although this eigenmode is less damped than in Case 1, its frequency remains the same, namely, $f = 214$ Hz.

(iii) Case 3: introduces $\omega^0 = 68.679 - 7.594\mathrm{i}$ in the DNS code using $X_e = 8$. The frequency shifts to $f = 364$ Hz, which is nearly identical to the first acoustic mode in the chamber, specifically, $f_{ac} = a_0/(4RX_e) = 363$ Hz.

The essential difference between the first two cases lies in the computations being carried out in chambers with slightly different lengths. In figure 4, one can clearly see that the mode $\omega = 40.409 - 9.164\mathrm{i}$, calculated for $X_e = 8$, shifts to $40.367 - 7.302\mathrm{i}$ when the length is increased to $X_e = 10$. Physically, the two modes are virtually the same and the lowest for the given geometry.

For the two chamber lengths, $X_e = 8$ and 10, the acoustic frequencies are 291 and 363 Hz, respectively. For Cases 1 and 2, the frequency of the intrinsic disturbance is 214 Hz, hence considerably lower than the acoustic mode frequency. Because of this disparity in frequencies, one expects the perturbations to exhibit linear oscillations. In contrast to the first two cases, Case 3 consists of an eigenmode with a frequency that mirrors the first acoustic mode. At the outset, one expects nonlinear interactions

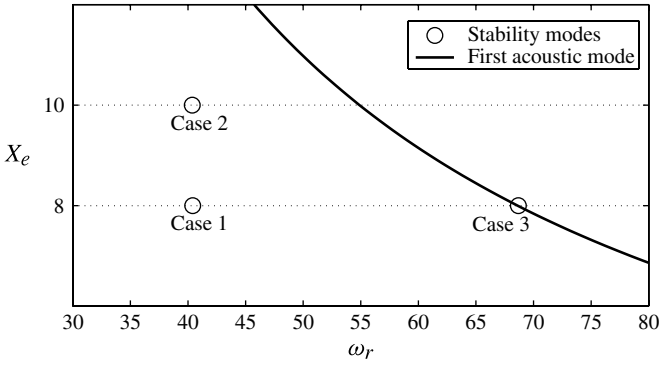

FIGURE 7. Sketch representing the three benchmark cases.

to be imminent. These three cases are situated side by side in figure 7, where both acoustic and stability eigenmode frequencies are displayed as function of the chamber length X_e.

Before additional comparisons could be made, a few definitions are in order. First, we introduce s^q_{fluc} as the net fluctuation in q reported by a virtual sensor signal. It is obtained by subtracting the mean flow from the DNS value at a sensor location. Second, we let s^q_{th} represent the theoretical evolution of q according to biglobal stability analysis as given by (3.6).

4.1.3. *Radial fluctuations*

Any signal s^q_{fluc} can be compared to its theoretical prediction s^q_{th}. Starting with the computed $s^{u_r}_{fluc}$ for the three representative cases, figures 8(*a*)–8(*c*) provide an overview of the results obtained for the radial velocity fluctuations.

As one may infer from figure 8(*a,b*), excellent agreement exists between DNS and biglobal stability solutions for the radial velocity in Cases 1 and 2. A short animation of the radial fluctuations obtained from the DNS signal $s^{u_r}_{fluc}$ for Case 1 is provided in supplementary movie 1, available online at http://dx.doi.org/10.1017/jfm.2012.245. Here, it can be clearly seen that $s^{u_r}_{fluc} \approx s^{u_r}_{th}$. This agreement is no longer valid for Case 3 in figure 8(*c*). This outcome is typical of other results obtained in our study as signals from other sensor locations lead to similar conclusions.

In principle, as long as an eigenmode's circular frequency remains sufficiently separated from an acoustic mode, its linear evolution predicted by linear stability theory appears to be quite accurate, being corroborated by DNS results. Indeed, only real parts $(\hat{u}_r)_r$ and $(\hat{u}_x)_r$ are introduced in the DNS code at $t = 0$ while the theoretical pattern in (3.6) also involves $(\hat{u}_r)_i$, ω_r and ω_i. Consequently, in addition to an already gratifying DNS confirmation of the values of ω_r and ω_i for a given eigenmode, the dependence of our stability results on X_e is also verified.

The remaining question is now turned to the physical interpretation of the dependence of eigenmodes on the domain size. It may be argued that truncating the cylinder at $x = X_e$ enables us to ignore the accelerating mean flow and its influence on the eigenmodes downstream of X_e. Then, given the nature of spatial amplification in the streamwise direction, we find that longer domain sizes lead to less damped and, hence, less stable eigenmodes.

Concerning Case 3, the fast Fourier transform (FFT) of the signal, $s^{u_r}_{fluc}$, can be used to track down the origin of the discrepancy observed in figure 8(*c*). However,

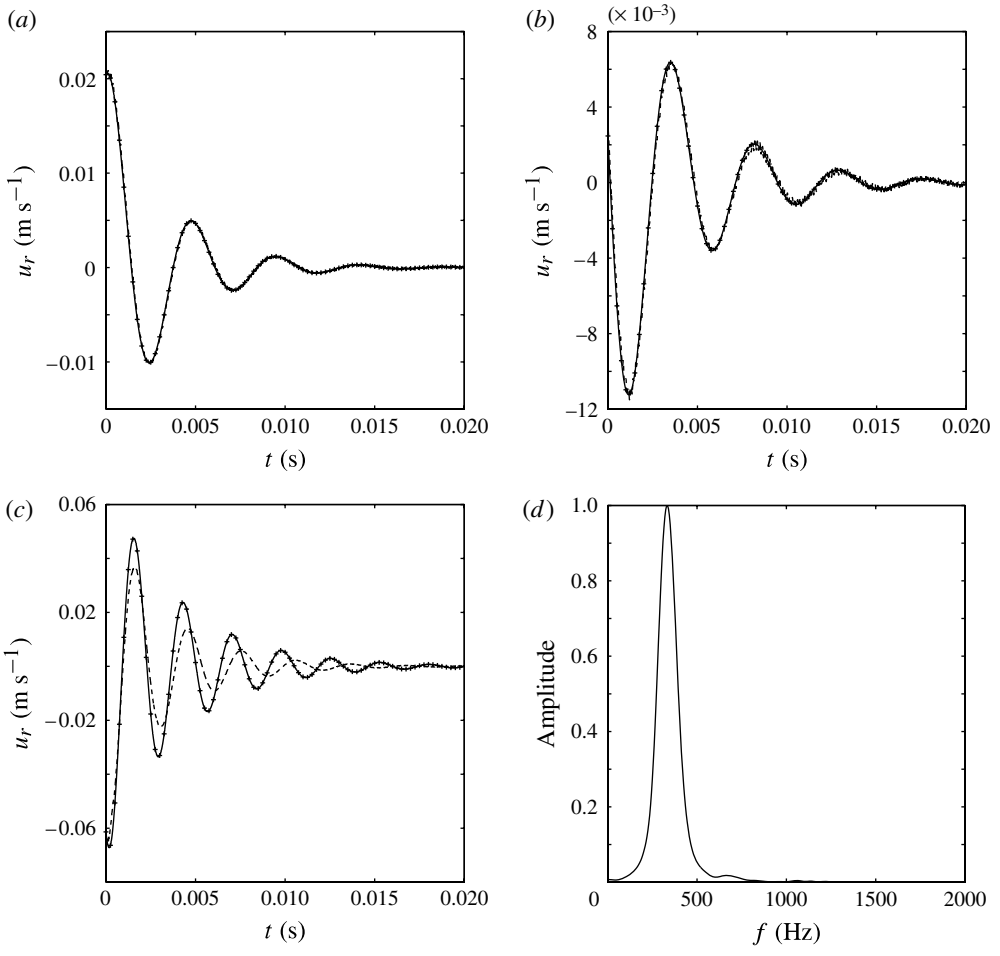

FIGURE 8. Comparisons between the fluctuating radial velocity signal $s^{u_r}_{fluc}$ (dashed line) and the theoretical evolution $s^{u_r}_{th}$ (solid line with + symbol) given by (3.6) for the three cases of figure 7: (*a*) u_r at $(x, r) = (7.333, 0.342)$, Case 1; (*b*) u_r at $(x, r) = (8, 0.809)$, Case 2; (*c*) u_r at $(x, r) = (8, 0.866)$, Case 3. (*d*) The FFT output for $s^{u_r}_{fluc}$ in (*c*), Case 3.

calculating the FFT of such signals proves to be laborious because our sampling frequency happens to be considerably high relative to the amplified frequencies. For this reason, the periodogram method with a Hann window is employed to acquire the frequency signature of the signal $s^{u_r}_{fluc}$.

The peak in figure 8(*d*) corresponds to $f = 335$ Hz, a value that matches the frequency of $\omega^{62} = 62.787 - 7.389\mathrm{i}$. This eigenmode happens to be the neighbouring point in figure 4 to the initially introduced $\omega^{68} = 68.679 - 7.594\mathrm{i}$.

At first glance, it may be surprising to identify ω^{62} in the DNS computations since its frequency lags behind the fundamental acoustic frequency by 30 Hz, whereas ω^{68} falls within 1 Hz of f_{ac}. Upon further inspection, it may be seen that the two eigenmodes are at play in this particular case. Given available signal characteristics, the low frequency accuracy achieved by the periodogram method does not allow us to conclude with absolute certainty that the only amplified frequency is $f = 335$ Hz. Moreover, neither the modal evolution $s^{u_r}_{th}$ of ω^{68} nor that of ω^{62} corresponds to the

acquired DNS signal $s^{u_r}_{fluc}$. At this point we realize that a combination of the two eigenmodes will lead to a more suitable fit.

To identify the individual modal contributions, a spatial decomposition over the acquired set of signals $s^{u_r}_{fluc}$ must be performed at each time step. To this end, each signal $s^{u_r}_{fluc}$ may be assumed to be a combination of the two eigenfunctions corresponding to ω^{68} and ω^{62}. Letting A^{68} and A^{62} be the complex amplitude coefficients of the combined signal (standing for the exponential dependence $Ae^{-i(V_{inj}/R)\omega t}$ in (3.6)), then $s^{u_r}_{fluc}$ may be deduced from the real part of the complex sum $A^{62}\hat{u}^{62} + A^{68}\hat{u}^{68}$, namely,

$$s^{u_r}_{fluc} = A^{62}_r\,(\hat{u}^{62}_r)_r - A^{62}_i\,(\hat{u}^{62}_r)_i + A^{68}_r\,(\hat{u}^{68}_r)_r - A^{68}_i\,(\hat{u}^{68}_r)_i\,. \tag{4.1}$$

At each time step, one has as many relations of the form given by (4.1) as the number of virtual sensor signals, namely 30. In view of this overdetermined system, the four unknowns $(A^{62}_r, A^{62}_i, A^{68}_r, A^{68}_i)$ are calculated using least squares. This enables us to fully recover the complex amplitude coefficients (A^{68}, A^{62}) as a function of time.

Figures 9(*a*)–9(*c*) display the modulus and phases of (A^{68}, A^{62}) and compare them to modal solutions based on the theoretical evolution prescribed by (3.6), i.e. the envelope $Ae^{\nu t}$. According to the resulting combination, the initially introduced eigenmode ω^{68} collapses at the very beginning of the computation in favour of ω^{62}. Thus, one can note the large gap that exists between the computed evolution of ω^{68} and its theoretical modal prediction $0.01A_0 \parallel (\hat{u}^{68}_r)_r \parallel_\infty e^{\nu^{68} t}$. In contrast, as shown in figure 9(*b*), ω^{62} tends to behave linearly following its quasi-modal evolution with a small phase gap. Similarly, as depicted in figure 9(*a*), its amplitude decreases according to modal behaviour of the form $A_1 e^{\nu^{62} t}$ with a proportionality constant $A_1 = 10$. In fact, this mode becomes dominant in the majority of the computations as confirmed by the frequency analysis of the signals: see figure 8(*d*). Instead of strong coupling between acoustic and stability modes, the present analysis suggests a probable pairing mechanism. For example, the velocity eigenfunctions $\hat{u_x}$ and $\hat{u_r}$ exhibit similar attributes for ω^{62} and ω^{68}. In particular, the corresponding peak values in $\hat{u_x}$ occur at the same location near the wall. Given this behaviour, we may be unable to ascertain whether the bimodal analysis supports the existence of a physical coupling mechanism or whether a numerical artefact is triggering a rather spurious, coupling-like effect due to the proximity of eigenmodes.

So far, in the analysis of $s^{u_r}_{fluc}$, no strong evidence of vorticoacoustic fluctuations has been seen. Upon a closer look, however, the absence of acoustic mode manifestation in the radial direction may be attributed to the amplitude of $\tilde{u}_r$ being small, specifically of $O(M)$ or 10^{-3} relative to $\tilde{u}_x$. Recalling that $\breve{u}_r = 0$ and $\tilde{u}_r \approx O(M\tilde{u}_x)$ in (3.12), it is no longer surprising that reconciliation between theory and DNS could be achieved in the case of radial fluctuations without reference to the vorticoacoustic field. Evidently, this situation changes in the analysis of axial fluctuations.

4.1.4. *Axial fluctuations*

Let us now examine the signals acquired for the axial fluctuations $s^{u_x}_{fluc}$. Unlike the analysis of radial disturbances, substantial discrepancies between $s^{u_x}_{fluc}$ and $s^{u_x}_{th}$ are observed for all three benchmark cases. Figures 10(*a*) and 10(*b*) provide examples for Cases 1 and 2. While the interplay of two eigenmodes may be responsible for part of the discrepancies associated with Case 3, the disagreement in Cases 1 and 2 between DNS and biglobal stability solutions can only be due to the omission of the vorticoacoustic contributions. This behaviour suggests a strong likelihood of acoustic

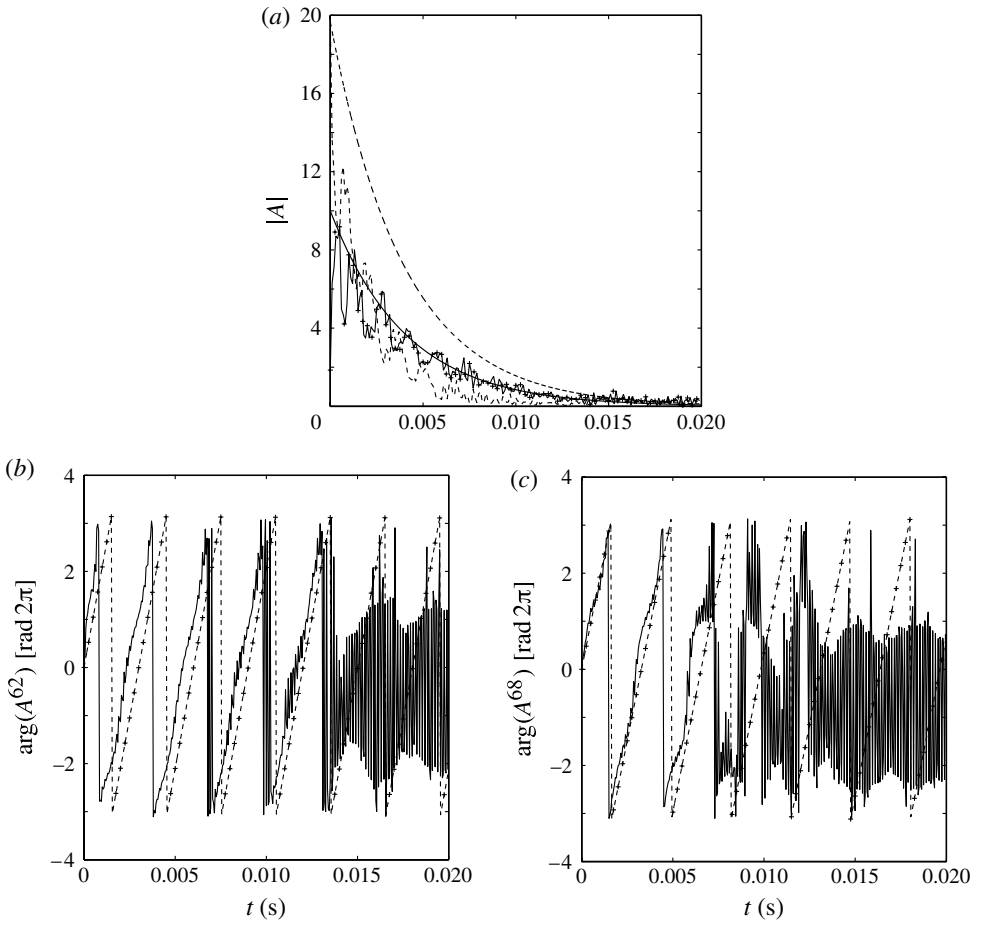

FIGURE 9. (*a*) The amplitude evolution for the two modes $\omega^{62} = 62.787 - 7.389\mathrm{i}$ (solid line with + symbol) and $\omega^{68} = 68.679 - 7.594\mathrm{i}$ (dashed line). These amplitudes are compared to $A_1 \mathrm{e}^{\nu^{62} t}$ (solid line) and $0.01 A_0 \parallel (\hat{u}_r^{68})_r \parallel_\infty \mathrm{e}^{\nu^{68} t}$ (dashed line). Amplitudes $|A_{62}|$ and $|A_{68}|$. (*b,c*) Comparison of the phase functions φ^{62} and φ^{68} (dashed lines) and the theoretical evolutions $2\pi f^{62} t[2\pi]$ and $2\pi f^{68} t[2\pi]$ (solid lines with + symbol): (*b*) φ^{62}; (*c*) φ^{68}.

modes developing naturally during the simulation, a hypothesis that will soon be tested.

For Cases 1 and 2, the acoustic part of the signal in $s^{u_x}_{fluc}$ can be extracted by subtracting the linear evolution $s^{u_x}_{th}$ using $s^{u_x}_{ac} = s^{u_x}_{fluc} - s^{u_x}_{th}$. The hydrodynamic and vorticoacoustic fluctuations can be identified in supplementary movie 2 which represents the DNS evolution of $s^{u_x}_{fluc}$ for Case 1. For Case 3, assuming a dual mode coupling, the acoustic part $s^{u_x}_{ac}$ may be restored from the pair of coefficients A^{62} and A^{68}. This is accomplished by taking

$$s^{u_x}_{ac} = s^{u_x}_{fluc} - A^{62}_r \, (\hat{u}^{62}_x)_r + A^{62}_i \, (\hat{u}^{62}_x)_i - A^{68}_r \, (\hat{u}^{68}_x)_r + A^{68}_i \, (\hat{u}^{68}_x)_i \, . \tag{4.2}$$

Here, the combination of acoustic modes can be readily evaluated owing to the closed-form analytical approximations provided in § 3.2.

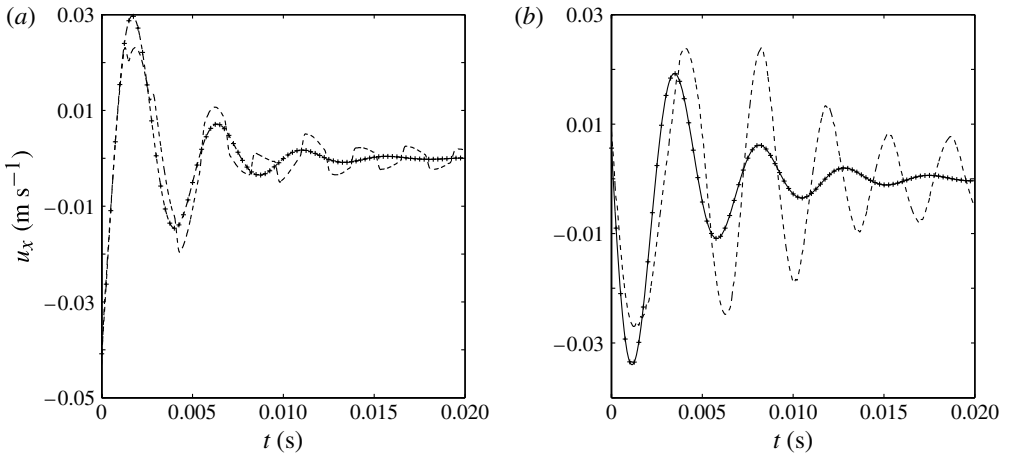

FIGURE 10. Comparisons between the fluctuating axial velocity signal $s^{u_x}_{fluc}$ (dashed line) and the theoretical evolution $s^{u_x}_{th}$ (solid line with + symbol) given by (3.6) for Cases 1 and 2: (*a*) u_x at $(x, r) = (7.333, 0.342)$, Case 1; (*b*) u_x at $(x, r) = (8, 0.809)$, Case 2.

Concerning the pressure oscillations, they are mainly composed of acoustic modes because any signal s^{p}_{fluc} remains chiefly prescribed by the acoustic waveform $\breve{p}$; the other two contributions $\hat{p}$ and $\tilde{p}$ may be ignored, being negligible in comparison. While the pseudopressure $\tilde{p}$ that accompanies the boundary-driven vorticoacoustic wave is known to be of higher order in the Mach number, the pressure fluctuation $\hat{p}$ proves to be immaterial, especially near the headwall of the chamber where the virtual pressure sensor is located. Since we essentially have $s^{p}_{fluc} \approx s^{p}_{ac}$, the signal s^{p}_{fluc} can be reconstructed from the first M acoustic modes using

$$s^{p}_{fluc} = \sum_{m=0}^{M} A_m \breve{p}_m, \tag{4.3}$$

where $\breve{p}_m = \cos(\omega_m x)\mathrm{e}^{-\mathrm{i}\omega_m t^*}$ corresponds to the plane wave given by § 3.2. Here too, we face an underdetermined system while writing (4.3) at each time step for the chosen sensor. This warrants the use of least squares to retrieve the coefficients $\{A_m\}$ of the combination of acoustic modes exhibiting a quasi-harmonic distribution with $A_m = 1/m^2$.

In view of A_m and the vorticoacoustic solution given by (3.12), the axial component of the acoustic mode fluctuation can be constructed and compared to $s^{u_x}_{ac}$ everywhere in the chamber. But first, the viscous dissipation mechanism that is present in the DNS results must be modelled and applied to the acoustic wave amplitudes. Otherwise, the inviscid amplitudes would remain constant and therefore insensitive to the amount of viscous dissipation in the chamber. In reality, acoustic amplitudes are susceptible to viscous decay and so this aspect must be modelled before meaningful comparisons can be made between DNS and theory.

Assuming linear acoustic oscillations for the three representative cases, an artificial function $F_\mu(t)$ is developed in a manner to match the observed viscous dissipation rate. We find $F_\mu(t) = F^0_\mu \mathrm{e}^{-2.3((V_{inj}t)/R_0)}$, with $F^0_\mu = 0.015$. It should be noted that $F_\mu(t)$ is used for all sensors and has the same expression for all three cases, despite the nonlinear interplay of eigenmodes that may be expected for Case 3. Furthermore, $F_\mu(t)$ is only

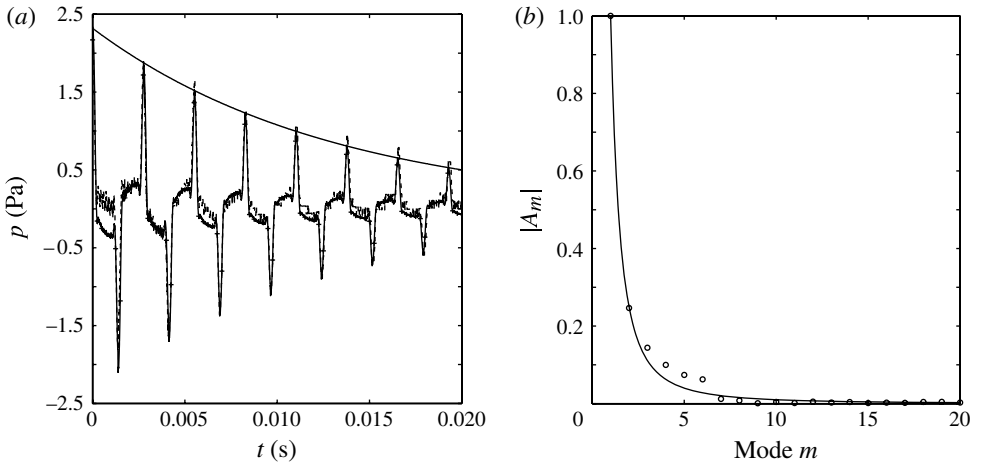

FIGURE 11. (*a*) Case 1 comparison between the signal s^p_{ac} (dashed line) and the combination of 100 acoustic modes (solid line with + symbol) for a sensor located at $(x, r) = (6.667, 0.985)$. The function F_μ (solid line) tracks the decaying envelope of the combined signal. (*b*) The circles show the values $\{A_m\}$ of the coefficients with respect to the mode number m. These are compared to the hyperbolic line $1/m^2$.

valid for $t > 0.005$ s, after the acoustic growth phase that occurs at the beginning of the computations.

A sample comparison between s^p_{ac} and the combination of acoustic modes is shown in figure 11(*a*). Since a combination of acoustic modes can reproduce the signal s^p_{ac} at any location in the chamber, this method can be used to faithfully predict the acoustic pressure. In figure 11(*b*), the coefficients $\{A_m\}$ are plotted with respect to the mode number m for the first 20 modes. Clearly, $A_m \approx 1/m^2$ and the combination found corresponds to a harmonic distribution of acoustic modes. The same coefficients $\{A_m\}$ can be relied upon to evaluate the vorticoacoustic velocity fluctuations $s^{ac}_{u_x}$.

Figures 12(*a*)–12(*d*) display comparative plots between DNS and biglobal stability solutions in which vorticoacoustic contributions and proper viscous dissipation are accounted for. The favourable agreement observed in figures 12(*a*)–12(*c*) is gratifying and lends support to the validity of our framework for Cases 1 and 2. It also confirms the accuracy of the vorticoacoustic approximation obtained by Majdalani and co-workers along with the suitability of a dissipation function to capture the effects of viscous attenuation on the acoustic modes.

The early disagreement between DNS and biglobal stability theory in figure 12(*d*) corresponds to Case 3, for which nonlinear pairing of eigenmodes is likely to occur. In this situation, the eigenmode coupling captured through (4.1) leads to good agreement, albeit limited to $t > 0.0055$ s. Other comparisons performed using several different DNS sensors lead to the same conclusion. As for the discrepancies observed in the first instants of figure 12(*d*), they are indicative of local nonlinear behaviour wherein the acoustic mode distribution captured through $\{A_m\}$ deviates from the expected harmonic form.

To summarize, both DNS and biglobal stability analysis converge in predicting the same dependence of eigenmodes on the size of the domain X_e. This is established through Cases 1 and 2 . In addition, introducing an eigenmode ω whose frequency is sufficiently removed from the acoustic modes leads to a conventional linear evolution

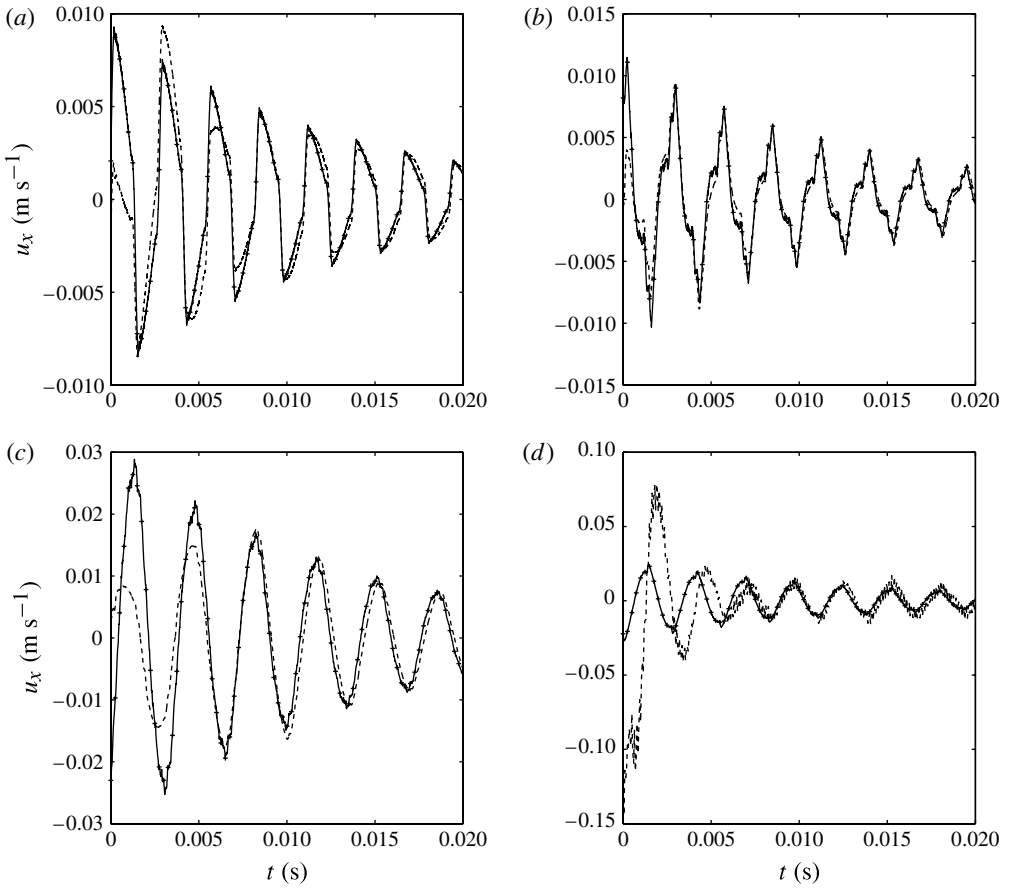

FIGURE 12. Comparisons between the acoustic part of longitudinal velocity signals $s_{ac}^{u_x}$ (dashed lines) and the acoustic reconstruction (solid lines with + symbol) based on the coefficients $\{A_m\}$ in (4.3) obtained from a pressure signal s_{fluc}^{p}. Viscous dissipation is modelled using $F_\mu(t)$. (*a*) u_x at $(x, r) = (7.333, 0.342)$, Case 1; (*b*) u_x at $(x, r) = (6.667, 0.985)$, Case 1; (*c*) u_x at $(x, r) = (8, 0.809)$, Case 2; (*d*) u_x at $(x, r) = (8, 0.866)$, Case 3.

that can be accurately predicted with the biglobal stability framework. In contrast, when the frequency of the introduced eigenmode happens to be close to an acoustic mode, a nonlinear mechanism occurs. Unlike the original eigenmode, a secondary one emerges naturally in the computed flow without being artificially superimposed. According to the present bimodal analysis, this natural emergence is linked to nonlinear interactions that give rise to internal, eigenmode-to-eigenmode pairing rather than external coupling between eigenmodes and acoustic modes.

4.2. *Dynamic cases*

In the second set of simulations, it is assumed that either R or V_{inj} are time-dependent. In real motors, the radius R continuously expands with respect to time due to propellant combustion and subsequent grain regression. However, in order to simplify the ensuing analysis, the sidewall boundary condition is specified with a temporal function $V_{inj}(t)$ while the mesh is kept unchanged with a fixed radius, $R = 0.03$ m. By varying $V_{inj}(t)$, we are able to simulate conditions leading to a

frequency shift according to $f = V_{inj}(t)\omega_r/(2\pi R)$. A frequency crossing is expected between an eigenmode and an acoustic mode. We hypothesize that such a crossing would trigger the emergence of a secondary eigenmode as seen in SRMs and VALDO experiments. Two main parameters characterize this crossing mechanism: the crossing speed linked to the slopes of the frequency evolutions and the minimal frequency gap for which the emergence of a secondary eigenmode can be induced. Realistic values of these parameters may be extracted from VALDO experiments and simulated in the DNS code. However, given the small time step $\Delta t = 5 \times 10^{-9}$ s used in our simulation, subsequent computations can be estimated to have prohibitively long durations. A compromise must be made and this is accomplished by taking

$$\begin{cases} X_e = 8 \ (0.24 \ \text{m}), \\ t \in [0, 0.06] \ (12\,000\,000 \text{ iterations}), \\ V_{inj}(t) = 0.98 + 0.5t. \end{cases} \tag{4.4}$$

By introducing into the DNS run the eigenmode $\omega^{68} = 68.679 - 7.594\text{i}$, its frequency $f = \omega_r^{68} V_{inj}(t)/(2\pi R)$ will range from 357 to 368 Hz during the computation, thus crossing at some point the first acoustic mode $f = 363$ Hz. In this manner, an amplification is expected to occur around $t = 0.04$ s. To engender secondary eigenmodes, the presence of small disturbances in the DNS code is required, and this effect may be realized through mesh deformation. To this end, the injection line is distorted such that $r = R + n(x)e^{-4}$, where $n(x)$ corresponds to 3 dB Gaussian white noise. The distortion is extended over the entire mesh using the radial function $\sin(\frac{1}{2}\pi r/R)$. This particular type of mesh deformation mainly affects the injection condition. A uniform wall-normal injection velocity V_{inj} gives rise to a non-uniform radial velocity $\bar{U}_r$ and a non-zero axial velocity $\bar{U}_x$. The induced shearing near the injecting wall becomes appreciable despite the mesh distortion being relatively small. It therefore leads to a high level of noise in the computations.

Using this mesh along with a constant injection velocity $V_{inj} = 0.98$ m s^{-1}, the steady-state motion is computed and used as the basic flow in the biglobal stability code. The eigenmodes are then modified. For example, $\omega^{68} = 68.679 - 7.594\text{i}$ is slightly distorted into $\omega^0 = 68.442 - 5.501\text{i}$. The slight shift in the circular frequency ω_r does not affect the upcoming frequency crossing. However, the reduction in $|\omega_i^0|$ makes this eigenmode less stable, especially in the presence of noise.

The other ingredient that is needed to induce the expected coupling is the inception of acoustic oscillations, particularly the first longitudinal modes, in the dynamic simulations. This may be accomplished by superimposing a harmonic distribution $1/m^2$ of the first ten acoustic modes onto the steady pressure field. The amplitude of the entire distribution is set at $0.001P_{atm}$, where P_{atm} is the atmospheric pressure imposed in the exit plane at $x = 8$. However, we find it unnecessary to add velocity perturbations to the steady-state velocities U_x and U_r.

Computations are initiated following this basic superposition. At the end of the simulation, signals from 100 virtual sensors are extracted. Then, using short-time Fourier transforms, our analysis is performed with a sampling frequency of $f_s = 10^5$ Hz.

Based on all sensors and signals for $s_{fluc}^{u_x}$, $s_{fluc}^{u_r}$ and s_{fluc}^{p}, the frequency analysis indiscriminately reveals a highly amplified frequency along with its nonlinear harmonics. The origin of this frequency, $f = 6050$ Hz, may be linked to the ninth acoustic mode $f_{ac} = 6180$ Hz. Nonetheless, limitations due to the sampling frequency and the relatively small number of sensors do not allow us to accurately analyse this

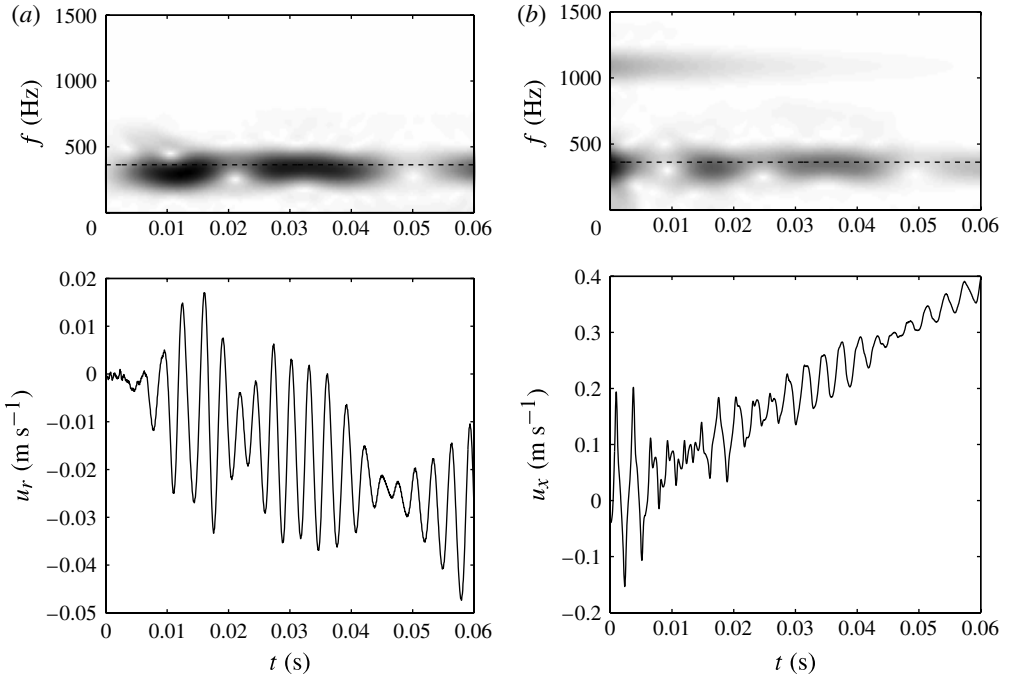

FIGURE 13. Evolutions of the filtered signals $s^{u_r}_{fluc}$ and $s^{u_x}_{fluc}$ and their short-time Fourier transforms (top). The horizontal dashed lines in the top part of each figure correspond to the first longitudinal acoustic mode frequency $f_{ac} = 363$ Hz. (*a*) u_r at $(x, r) = (7.222, 0.707)$; (*b*) u_x at $(x, r) = (8, 0.809)$.

mode. Its presence is eliminated by conditioning the signals using a Butterworth filter of order five and a cutting frequency of $f_c = 2000$ Hz. Furthermore, the continuous parts of the signals for $V_{inj}(t)s^q_{fluc}(0)/0.98$, which are linked to the increase in V_{inj}, are subtracted from the filtered signals.

We examine the radial and axial velocity fluctuations by showing in figures 13(*a*) and 13(*b*) samples of $s^{u_r}_{fluc}$ and $s^{u_x}_{fluc}$ at two sensor locations. As explained before, the radial disturbances are primarily composed of eigenmodes because their vorticoacoustic parts are negligible. Interestingly, figure 13(*a*) shows amplified frequencies around the first acoustic mode $f_{ac} = 363$ Hz. Furthermore, within the periodic signal for $s^{u_r}_{fluc}$, two distinct oscillations are observed, namely, around $t = 0.015$ and 0.03 s. These two oscillations correspond to the evolution of two eigenmode frequencies according to $f = (V_{inj}/2\pi R)\omega^0$. These are $\omega^{62} = 62.288 - 5.328$i and the expected eigenmode $\omega^{68} = 68.442 - 5.501$i. Figure 13(*b*) again shows the emergence of these two eigenmodes. In fact, after the first instants where the acoustic frequencies dominate the evolution of $s^{u_x}_{fluc}$, the signal begins to exhibit the two characteristic oscillations caused by the emergence of ω^{62} and ω^{68}.

Instead of the unique appearance of ω^{68} around $t = 0.04$ s, the DNS computations reveal the eigenmode ω^{62} around $t = 0.015$ s, prior to the anticipated appearance of ω^{68} around $t = 0.03$ s. The temporal stability of these modes is visible especially for ω^{68}, which quickly vanishes as its circular frequency moves away from the acoustic value.

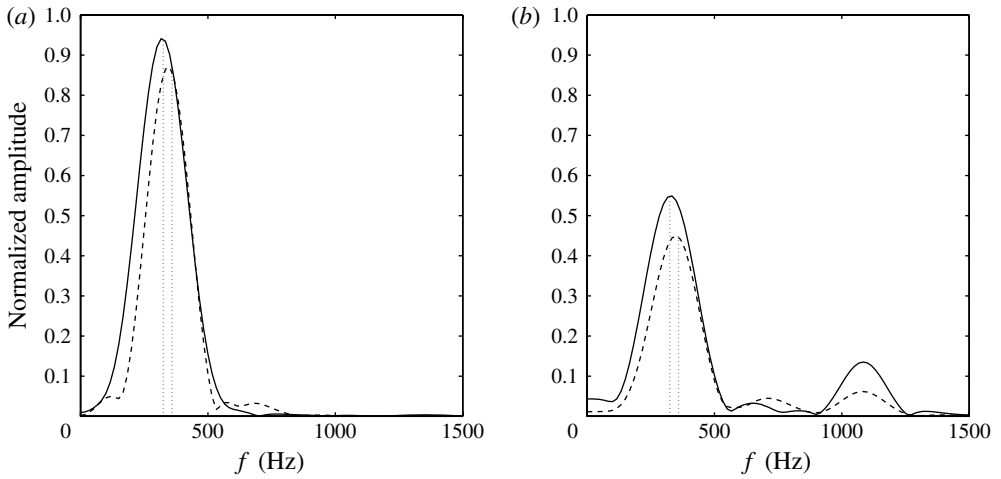

FIGURE 14. Spectra extracted from the short-time Fourier transforms of figure 13(*a,b*) at two distinct instants. Solid lines correspond to $t = 0.015$ s whereas dashed lines stand for $t = 0.03$ s. Vertical lines indicate frequencies of eigenmodes ω^{62} and ω^{68}. (*a*) u_r at $(x, r) = (7.222, 0.707)$; (*b*) u_x at $(x, r) = (8, 0.809)$.

Confirmation of the presence of the two eigenmodes is given by figures 14(*a*) and 14(*b*), where spectra at instants $t = 0.015$ s and $t = 0.03$ s are depicted. The amplitudes of signals $s^{u_r}_{fluc}$ and $s^{u_x}_{fluc}$ are normalized by the maximum values gained on the short-time Fourier transforms of figure 13(*a,b*). The reason for the appearance of ω^{62} is not entirely clear. However, as in the static simulation of Case 3, a nonlinear interaction between the first acoustic mode and the superimposed mode ω^{68} can trigger the emergence of the secondary eigenmode, ω^{62}.

In closing, it may be worthwhile to remark that, although our computations have been subject to a very fast crossing speed (i.e. 182 Hz s^{-1} compared to 34 Hz s^{-1} in the VALDO experiments), the main objective of this investigation has been achieved. The emergence of an eigenmode induced by the crossing of its frequency with an acoustic mode has been clearly demonstrated using both static and dynamic simulations. This behaviour constitutes a major result that lends support to our fundamental hypothesis for the occurrence of thrust oscillations in SRMs (see Chedevergne *et al.* 2006). The suspected coupling mechanism between acoustic modes and eigenmodes is now elucidated through the use of DNS data and biglobal stability theory.

5. Concluding remarks

In this study, we have shown that the use of DNS calculations can provide new physical insight into understanding the results of biglobal stability analysis. For example, we have demonstrated that the critical eigenvalues precipitated by the theoretical stability analysis are recovered when computing the unsteady motion of an isolated fluctuation through DNS calculations. In the process, special attention has been given to the dependence of the temporal growth rate ω_i on the chamber length X_e. Evidently, ω_i controls the stability character of these eigenmodes and the linear analysis predicts a growth in ω_i with successive increases in X_e. These theoretical results are limited to the use of a steady, laminar mean flow. Experimentally, this

assumption holds true as long as $x < 12$. Under these conditions, ω_i remains negative, thus implying the presence of temporal damping. However, as X_e continues to increase, nonlinearities in the flow will inevitably lead to strong amplification in the streamwise direction. The natural transition of the flow around $x = 12$ is likely to result from the existence of the eigenmodes discussed heretofore. This hypothesis has to be further explored in future work. So far, comparisons with cold and reactive gas experiments have confirmed the relevance of biglobal stability analysis in accurately estimating the temporally stable modes (see Chedevergne *et al.* 2006; Chedevergne & Casalis 2006*a*). The nature of these intrinsic instabilities has led to a coherent construct that explains the source of SRM thrust oscillations.

In addition to their important role in corroborating the biglobal stability results, these DNS calculations have confirmed the accuracy of Majdalani's analytical solution for the vorticoacoustic boundary-driven waves associated with the Taylor–Culick flow. Moreover, it has been demonstrated that the proximity of instability frequencies to natural acoustic modes can lead to the emergence of neighbouring stability eigenmodes. Both static and dynamic DNS computations made with a time-dependent injection velocity have established the presence of strong coupling between acoustic modes and instability eigenmodes. For the unsteady injection velocity cases, the frequency of one mode $f = V_{inj}\omega_r/(2\pi R)$ becomes a function of the time t and can cross the acoustic mode f_{ac}. This event reproduces what occurs in live motors, where the coupling mechanism between acoustics and intrinsic instabilities is believed to be responsible for the emergence of secondary eigenmodes and the merging of frequency paths.

Acknowledgements

This study was supported by the French Space Agency CNES and by ONERA. The authors thank M. Prévost and G. Avalon from ONERA for their accurate measurements, help, and valuable suggestions. The corresponding author was supported by the National Science Foundation.

Supplementary material

For supplementary material for this article, please visit http://dx.doi.org/10.1017/jfm.2012.245.

REFERENCES

ABU-IRSHAID, E. M., MAJDALANI, J. & CASALIS, G. 2007 Hydrodynamic stability of rockets with headwall injection. *Phys. Fluids* **19** (2), 024101.

APTE, S. & YANG, V. 2001*a* Unsteady flow evolution in a porous chamber with surface mass injection. Part 1. Free oscillation. *AIAA J.* **39** (8), 1577–1586.

APTE, S. & YANG, V. 2001*b* Unsteady flow evolution in porous chamber with surface mass injection. Part 2. Acoustic excitation. *AIAA J.* **40** (2), 244–253.

APTE, S. & YANG, V. 2003 A large-eddy simulation study of transition and flow instability in a porous-walled chamber with mass injection. *J. Fluid Mech.* **477**, 215–225.

AVALON, G., CASALIS, G. & GRIFFOND, J. 1998 Flow instabilities and acoustic resonance of channels with wall injection. In *34th AIAA/ASME/SAE/ASEE Joint Propulsion Conference and Exhibit*, AIAA Paper 98-3218.

AVALON, G. & JOSSET, T. 2006 Cold gas experiments applied to the understanding of aeroacoustic phenomena inside solid propellant boosters. In *42nd AIAA/ASME/SAE/ASEE Joint Propulsion Conference and Exhibit*, AIAA Paper 2006-5111.

BEDDINI, R. A. 1986 Injection induced flows in porous-walled ducts. *AIAA J.* **24** (11), 1766–1773.

BERMAN, A. 1953 Laminar flow in channels with porous walls. *J. Appl. Phys.* **24** (9), 1232–1235.

CASALIS, G., AVALON, G. & PINEAU, J.-P. 1998 Spatial instability of planar channel flow with fluid injection through porous walls. *Phys. Fluids* **10** (10), 2558–2568.

CASALIS, G., CHEDEVERGNE, F., FÉRAILLE, T. & AVALON, G. 2004 Global stability of the flow induced by wall injection. In *IUTAM Symp. Laminar–Turbulent Transition, Bangalore, India* (ed. R. Govindarajan). Springer.

CHEDEVERGNE, F. & CASALIS, G. 2005 Thrust oscillations in reduced scale solid rocket motors. Part 2. A theoretical approach. In *41st AIAA/ASME/SAE/ASEE Joint Propulsion Conference and Exhibit*, AIAA Paper 2005-4000.

CHEDEVERGNE, F. & CASALIS, G. 2006*a* Detailed analysis of the thrust oscillations in reduced scale solid rocket motors. In *42nd AIAA/ASME/SAE/ASEE Joint Propulsion Conference and Exhibit*, AIAA Paper 2006-4424.

CHEDEVERGNE, F. & CASALIS, G. 2006*b* Front wall boundary layer influence on the stability of the flow induced by wall injection. In *7th ONERA DLR Aerospace Symp, Toulouse, France*.

CHEDEVERGNE, F., CASALIS, G. & FÉRAILLE, T. 2006 Biglobal linear stability analysis of the flow induced by wall injection. *Phys. Fluids* **18** (1), 014103.

CHU, B.-T. & KOVÁSZNAY, L. S. G. 1958 Non-linear interactions in a viscous heat-conducting compressible gas. *J. Fluid Mech.* **3** (5), 494–514.

COUTON, D., DOAN-KIM, S. & VUILLOT, F. 1997 Numerical simulation of vortex-shedding phenomenon in a channel with flow induced through porous wall. *Intl J. Heat Fluid Flow* **18** (3), 283–296.

CULICK, F. E. C. 1966 Rotational axisymmetric mean flow and damping of acoustic waves in a solid propellant rocket. *AIAA J.* **4** (8), 1462–1464.

CULICK, F. E. C. 1968 A review of calculations for unsteady burning of a solid propellant. *AIAA J.* **6** (12), 2241–2254.

DUNLAP, R., BLACKNER, A. M., WAUGH, R. C., BROWN, R. S. & WILLOUGHBY, P. G. 1990 Internal flow field studies in a simulated cylindrical port rocket chamber. *J. Propul. Power* **6** (6), 690–704.

FABIGNON, Y., DUPAYS, J., AVALON, G., VUILLOT, F., LUPOGLAZOFF, N., CASALIS, G. & PRÉVOST, M. 2003 Instabilities and pressure oscillations in solid rocket motors. *Aero. Sci. Technol.* **7** (3), 191–200.

GOLUB, G. H. & LOAN, C. F. VAN. 1996 *Matrix Computations*, 3rd edn. The Johns Hopkins University Press.

GRIFFOND, J. 2002 Receptivity and aeroacoustic resonance in channels with blowing walls. *Phys. Fluids* **14** (11), 3946–3962.

GRIFFOND, J. & CASALIS, G. 2000 On the dependence on the formulation of some nonparallel stability approaches applied to the Taylor flow. *Brief Comm. Phys. Fluids* **12** (2), 466–468.

GRIFFOND, J. & CASALIS, G. 2001 On the nonparallel stability of the injection induced two-dimensional Taylor flow. *Phys. Fluids* **13** (6), 1635–1644.

GRIFFOND, J., CASALIS, G. & PINEAU, J. P. 2000 Spatial instability of flow in a semiinfinite cylinder with fluid injection through its porous walls. *Eur. J. Mech.* B **19** (1), 69–87.

KUENTZMANN, P. 1991 *Combustion Instabilities, AGARD*, vol. LS 180. AGARDograph.

KURDYUMOV, V. N. 2008 Viscous and inviscid flows generated by wall-normal injection into a cylindrical cavity with a headwall. *Phys. Fluids* **20** (12), 123602.

LEE, Y. & BEDDINI, R. A. 1999 Acoustically-induced turbulent transition in solid propellant rocket chamber flow fields. In *35th AIAA/ASME/SAE/ASEE Joint Propulsion Conference and Exhibit*, AIAA Paper 99-2508.

LEE, Y. & BEDDINI, R. A. 2000 Effect of solid rocket chamber pressure on acoustically-induced turbulent transition. In *36th AIAA/ASME/SAE/ASEE Joint Propulsion Conference and Exhibit*, AIAA Paper 2000-3802.

LUPOGLAZOFF, N. & VUILLOT, F. 1996 Parietal vortex shedding as a cause of instability for long solid propellant motors: numerical simulations and comparisons with firing tests. In *34th Aerospace Sciences Meeting and Exhibit*, AIAA Paper 96-0761.

MAJDALANI, J. 1998 A hybrid multiple scale procedure for boundary layers involving several dissimilar scales. *Z. Angew. Math. Phys.* **49** (6), 849–868.

MAJDALANI, J. 1999 The boundary layer structure in cylindrical rocket motors. *AIAA J.* **37** (4), 505–508.

MAJDALANI, J., FLANDRO, G. & ROH, T. 2000 Convergence of two flowfield models predicting a destabilizing agent in rocket combustion. *J. Propul. Power* **16** (3), 492–497.

MAJDALANI, J. 2001*a* The oscillatory channel flow with arbitrary wall injection. *Z. Angew. Math. Phys.* **52** (1), 33–61.

MAJDALANI, J. 2001*b* Vorticity dynamics in isobarically closed porous channels. Part I: standard perturbations. *J. Propul. Power* **17** (2), 355–362.

MAJDALANI, J. 2007 On steady rotational high speed flows: the compressible Taylor–Culick profile. *Proc. R. Soc.* A **463** (2077), 131–162.

MAJDALANI, J. 2009 Multiple asymptotic solutions for axially travelling waves in porous channels. *J. Fluid Mech.* **636** (1), 59–89.

MAJDALANI, J. & AKIKI, M. 2010 Rotational and quasiviscous cold flow models for axisymmetric hybrid propellant chambers. *Trans. ASME: J. Fluids Engng* **132** (10), 101202.

MAJDALANI, J. & FLANDRO, G. A. 2002 The oscillatory pipe flow with arbitrary wall injection. *Proc. R. Soc.* A **458** (2022), 1621–1651.

MAJDALANI, J. & RIENSTRA, S. W. 2002 Two asymptotic forms of the rotational solution for wave propagation inside viscous channels with transpiring walls. *Q. J. Mech. Appl. Math.* **55** (1), 141–162.

MAJDALANI, J. & ROH, T. S. 2000 The oscillatory channel flow with large wall injection. *Proc. R. Soc.* A **456** (1999), 1625–1657.

MAJDALANI, J. & VAN MOORHEM, W. K. 1998 Improved time-dependent flow field solution for solid rocket motors. *AIAA J.* **36** (2), 241–248.

MAJDALANI, J., VYAS, A. B. & FLANDRO, G. A. 2002 Higher mean-flow approximation for a solid rocket motor with radially regressing walls. *AIAA J.* **40** (9), 1780–1788.

MAJDALANI, J., VYAS, A. B. & FLANDRO, G. A. 2009 Higher mean-flow approximation for a solid rocket motor with radially regressing walls: erratum. *AIAA J.* **47** (1), 286–286.

PRÉVOST, M. & GODON, J. CL. 2005 Thrust oscillations in reduced scale solid rocket motors. Part 1. Experimental investigations. In *41st AIAA/ASME/SAE/ASEE Joint Propulsion Conference and Exhibit*, AIAA Paper 2005-4003.

REFLOCH, A., COURBET, B., MURRONE, A., VILLEDIEU, P., LAURENT, C., GILBANK, P., TROYES, J., TESSÉ, L., CHAINERAY, G., DARGAUD, J. B., QUÉMERAIS, E. & VUILLOT, F. 2011 CEDRE software. *The ONERA J., AerospaceLab* **2**, http://www.aerospacelab-journal.org.

TAYLOR, G. I. 1956 Fluid flow in regions bounded by porous surfaces. *Proc. R. Soc.* A **234** (1199), 456–475.

THEOFILIS, V. 2003 Advances in global linear instability analysis of nonparallel and three-dimensional flows. *Prog. Aerosp. Sci.* **39** (4), 249–315.

THEOFILIS, V. 2011 Global linear instability. *Annu. Rev. Fluid Mech.* **43**, 319–352.

THEOFILIS, V., DUCK, P. W. & OWEN, J. 2004 Viscous linear stability analysis of rectangular duct and cavity flows. *J. Fluid Mech.* **505**, 249–286.

UGURTAS, B., AVALON, G., LUPOGLAZOFF, N. & VUILLOT, F. 1999 Numerical computations of hydrodynamic instabilities inside channels with wall injection. In *35th AIAA/ASME/SAE/ASEE Joint Propulsion Conference and Exhibit*, AIAA Paper 99-2505.

VARAPAEV, V. N. & YAGODKIN, V. I. 1969 Flow stability in a channel with porous wall. *Fluid Dyn. (Izv. Akad. Nauk SSSR Mekh. Zhidk. Gaza)* **4** (5), 91–95.

VUILLOT, F. 1995 Vortex shedding phenomena in solid propellant motors. *J. Propul. Power* **11** (4), 626–639.

VUILLOT, F., SCHERRER, D. & HABIBALLAH, M. 2003 CFD code validation for space propulsion applications. In *5th Int. Symp. Liquid Space Prop. Chattanooga, Tennessee*. NASA Marshall Space Flight Center.